Enhancing Downlink QoS and Energy Efficiency through a User-Centric Stienen Cell Architecture for mmWave Networks

Umair Sajid Hashmi[*], Syed Ali Raza Zaidi[†], Ali Imran[‡] and Adnan Abu-Dayya[§]

[*]School of Electrical Engineering and Computer Science (SEECS), National University of Sciences and Technology (NUST), Islamabad, Pakistan. [†]School of Electronic and Electrical Engineering, University of Leeds, Leeds LS2 9JT, U.K. [‡]AI4Networks Lab, School of Electrical and Computer Engineering, University of Oklahoma, Tulsa, OK, USA. [§]Qatar Mobility Innovations Center, P.O. Box 210531, Doha, Qatar. Corresponding author: umair.hashmi@seecs.edu.pk

Abstract

This paper presents an analytical framework for performance characterization of a novel Stienen cell based user-centric architecture operating in millimeter wave spectrum. In the proposed architecture, at most one remote radio head (RRH) is activated within non overlapping user equipment (UE)-centric Stienen cells (S-cells) generated within the Voronoi region around each UE. Under the presented framework, we derive analytical models for the three key performance indicators (KPIs): i) SINR distribution (used as an indicator for quality of service (QoS)), ii) area spectral efficiency (ASE), and iii) energy efficiency (EE) as a function of the three major design parameters in the proposed architecture, namely UE service probability, S-cell radius coefficient and RRH deployment density. The analysis is validated through extensive Monte Carlo simulations. The simulation results provide practical design insights into the interplay among the three design parameters, tradeoffs among the three KPIs, sensitivity of each KPI to the design parameters as well as optimal range of the design parameters. Results show that compared to current non user-centric architectures, the proposed architecture not only offers significant SINR gains, but also the flexibility to meet diverse UE specific QoS requirements and trade between EE and ASE by dynamically orchestrating the design parameters.

Index Terms

User-Centric Architectures, Stienen Model, Area Spectral Efficiency, Energy Efficiency.

I. INTRODUCTION

Ultra-dense deployment of small cells using higher frequency bands, such as millimeter wave (mmWave), is being widely accepted in both academia and industry as the prime course to meet

the ever growing data demands in future cellular networks, vis-a-vis 5G and beyond. Unlike some earlier studies, it has now been established that densification alone does not yield linear gains in coverage probability. In fact, the coverage probability shows a decreasing trend at high base station (BS) densities as the network transitions from a noise-limited to an interference-limited system [1]. To aggravate matters further, high operational expenditures and energy consumption associated with dense deployments take a toll on the network operators by further reducing the already dwindling profit margins.

Designing and operating the network in a user equipment (UE)-centric fashion instead of the traditional cell-centric design has gained traction recently as a viable strategy for 5G and beyond [2]. Shifting the network design pivot from the BS to the UE not only ensures ubiquitous coverage and UE specific differentiated quality of service (QoS) to the UEs in dense deployments, but also provides a mechanism for selective BS activation that ensures reduced energy consumption. Recent works have quantified the area spectral efficiency (ASE) and energy efficiency (EE) in a user-centric Cloud radio access network (C-RAN) [3], [4], [5]. The network design in both these works relies upon creating non-overlapping circular service zones around high priority UEs. This results in a one-to-one (1-1) UE-BS association for each service zone such that a single BS is activated at max per service zone. The service zone radius is employed as a control parameter to realize the desired tradeoff between EE and ASE. However, the disjoint circular user-centric service zones in the mentioned works cause high latency, specially within dense user hotspots, due to longer wait times in downlink (DL) scheduling.

In this paper, we propose and analyze a novel user-centric architecture based on Stienen cells around UEs for downlink scheduling in ultra-dense deployment scenarios. The Stienen model, introduced in 1982 [6] considers the maximal ball inscribed within the Poisson Voronoi cell and centered at the generating point of the Voronoi cell. In simple terms, Stienen model is formed by non overlapping circular cells around UEs selected for downlink scheduling. The diameter of those circular regions (or Stienen cells) has the exact same distribution as the nearest neighbor distance of a Poisson point process. In the proposed architecture, all the BSs within a UE-centric Stienen cell (S-cell) are associated to its centroid UE. The Stienen cells are bounded by the Voronoi tessellation generated through the UE positions on the x-y plane (see Fig. 1). The Stienen model offers manifold advantages compared to the already conceived user-centric architectures: i) it integrates the randomness in BS deployment as well as user locations, ii) it enables flexibility to capture the effect of polygonal user-centric service regions, something that

the one-size-fits-all strategy fails to do, and iii) it gives an opportunity for all the UEs to be scheduled, provided the BS deployment is sufficiently dense to ensure presence of at least one BS within each UE-centric S-cell.

By employing stochastic geometry principles, we obtain the analytical framework to determine the coverage bounds in the proposed user-centric Stienen architecture. While deployment of a large number of BSs is capable of enhancing coverage for an arbitrary UE, the energy consumption becomes significant. Our model tackles the dual problem of maintaining high throughput as well as energy efficiency through the selective BS activation mechanism. We consider operating activated BSs within S-cells at high frequency mmWave band on DL because: i) experimental trials have indicated suitability of mmWave communications due to high spectrum availability per channel [7]; ii) higher frequencies allow implementation of small-sized antenna arrays to facilitate narrow directional beams and longer transmission ranges; and iii) larger free space pathloss and directional DL transmissions at mmWave frequencies reduce the unwanted interference from nearby BSs. Additionally, the UE-BS pair proximity within the Stienen model ensures resilience to blockage effects that occur at larger UE-BS distances. Furthermore, since the mmWave cells do not interfere with existing sub-6 GHz BSs, they can be deployed within existing deployments and enable architectures such as Cloud RAN enabled heterogeneous networks and control-data separation architecture (CDSA) [8].

A. KPIs and Design parameters

The main aim of this work is the analytical quantification and analysis of a novel user-centric Stienen cell model for dense mmWave cellular networks. The analysis is carried out in terms of three KPIs: i) UE SINR distribution, ii) ASE, and iii) EE. The SINR distribution allows us to analyze and compare an arbitrarily scheduled UE's QoS with other models. Our cell design and scheduling scheme targets reduction in interference at the UE which subsequently allows higher achievable throughputs. Reduction in interference increases achievable throughput for an arbitrary UE, but does it also increase sum throughput in the network? The answer to this lies in the analysis of ASE measure which is a function of both per user SINR and average number of scheduled UEs per scheduling time instance. The final KPI is basically a benefit-cost ratio, where the benefit is the network spectral efficiency and the cost is given by the network power consumption per unit area. In a multi-tier network, EE will depend upon the number of activated mmWave RRHs. As we supplement the sub-6 GHz MBS with activated mmWave RRHs, the EE is expected to improve initially because of higher data rates at UEs connected to nearby mmWave

RRHs. However, if we keep on activating mmWave RRHs, then after a certain sweet point, the EE tapers off and eventually reduces because the power consumption cost will overshadow the spectral efficiency improvement.

We analyze and optimize the aforementioned KPIs using three key design parameters namely: 1) the active UE population, 2) Stienen cell size factor and 3) mmWave RRH deployment density. The active UE population denotes the percentage of UEs that participate in the DL scheduling process, hence determining the average geometry of the S-cell network. If this percentage of participating UEs is low, the average separation between UEs is increased, thereby also increasing the mean of Stienen cell sizes around UEs. Another consequence is the increase in probability for an arbitrary UE to be scheduled via mmWave RRHs in a fixed RRH deployment. The Stienen cell size factor is simply a parameter that varies between 0 and 1. A factor of 1 indicates that the Stienen cell is at the largest allowable size and inscribed within the user-centric Voronoi cell. Variations in this parameter effect the UE load distribution between the MBS and RRH tiers and consequentially impact the ASE and EE. Finally, a higher mmWave RRH deployment density also causes a larger number of UEs to be connected to the RRHs, which increases the spectral efficiency but reduces EE owing to increased RRH power consumption.

B. Related Work

There has been notable work in recent literature focusing on the benefits of restructuring the network design around the UE. Authors in [2] offer a comprehensive literature on the concept of user-centric ultra dense networks and the *de-cellular* idea. The framework for access point grouping is presented that allows the network to follow the user seamlessly regardless of user location and movement. The challenges associated with such a network in terms of mobility, resource and interference management are elaborated in comparison to the current cell-centric networks such as 4G. Authors in [9] introduce the concept of a virtual user-centric C-RAN cell design, wherein a user is the center of a circular virtual cell served by multiple remote radio heads (RRHs) simultaneously. Optimal power control in the form of maximum ratio transmission (MRT) is used at BSs, which makes the analysis different from that based on standard Poisson point process. Unlike [9], where the proposed RRH clustering is overlapping (scenarios where a single RRH may simultaneously serve multiple UEs), our model builds on non-overlapping user-centric S-cells resulting in a one-to-one UE-RRH association during a given time slot.

The application of user-centric architectures has also been studied in relevance with upcoming 5G technologies, that include transmission in mmWave spectrum, use of massive MIMO de-

ployment and 3GPP's 5G New Radio (NR) standard. Authors in [10] developed an optimization framework for power control strategies aimed at maximizing throughput fairness or the sum rate in cell free massive MIMO systems. A comparison with user-centric architecture within the designed system model demonstrated performance gains for both the cases of uniform power allocation and sum-rate maximizing power allocation. The extension of this work is carried out in [11], where the authors addressed the problem of power control for cell-free and user-centric architecture at mmWave frequencies. Recent studies [12][13] formulate the closed form expressions for spectral and energy efficiencies by taking into account both the base station transmit power and deployment density. The interplay between transmit power and base station density is characterized within the cell association phase in the expression for coverage probability. While these studies present valuable models for dense conventional deployments, we choose energy models that support centralized processing for dynamic activation / deactivation of mmWave RRHs in the proposed user-centric Stienen model (more on this in Section VI).

The only work that considers Stienen based model for stochastic geometry analysis of wireless networks is [14], in which the authors characterize the coverage, throughput and energy efficiency in non-uniform two-tier networks. All the users within the MBS centered S-cells are associated with the respective MBS, while UEs in the Voronoi cell region outside the S-cell are associated with the closest femto base station. While our work also utilizes Stienen based network modeling, it is distinct from [14] in following fundamental ways. Contrary to [14], wherein the Stienen cells are centered on MBS, we propose and analyze an architecture where the center of the S-cell is an active UE. Secondly, in [14], analysis is focused only on sub-6 GHz band, whereas, in our model, each active UE is connected with a mmWave RRH, given there is at least one RRH present within its S-cell, otherwise the UE connects to the closest MBS (in case of multi-tier networks). Ultimately, the overarching goal of this work is to evaluate the performance gains offered by a Stienen model in a user-centric dense mmWave network in terms of three key performance indicators (KPIs): i) ASE, ii) EE, and iii) user QoS.

C. Contributions and Paper Arrangement

The preceding discussion shows that user-centric architectures have been well investigated for both mmWave and sub-6 GHz deployments. However, to the best of the authors' knowledge, analytical characterization and performance analysis of the Stienen based model in user-centric mmWave network remains terra incognita. Through our investigation towards the relevance of

this system model in future ultra dense 5G networks, we are attempting to close this research gap. To this end, the main contributions of this work are summarized as follows:

- *Stienen model based user-centric architecture:* We first introduce the user-centric S-cell model and the UE-RRH association mechanism. We incorporate the idiosyncrasies related with mmWave communication in our system model. These include the impact of shadowing on channel characteristics, pathloss disparity for line-of-sight (LOS) and non-line-of-sight (NLOS) scenarios and impact on signal-to-interference-plus-noise ratio (SINR) due to directional coverage.

- *Characterization of the distance to nearby angularly interfering RRHs:* Based on the presented framework, we investigate the spatial repulsion induced between a UE and the activated mmWave RRHs outside the UE's S-cell with highly aligned directional transmission beams (such RRHs are referred henceforth as angularly interfering RRHs). Due to maximum transmission gain, the interference from angularly interfering RRHs will dominate the interference from non-aligned interfering RRHs. An example of a UE-angularly interfering RRH pair is given by the red dotted line in Fig. 1. To model the spatial proximity and density of angularly interfering RRHs around a UE, we introduce a UE service selectivity parameter which is the proportion of UEs considered for service during each DL scheduling slot. A low selectivity parameter results in a larger average S-cell radius, which ensures spatial repulsion between a UE and its angularly interfering RRHs at the cost of longer scheduling wait times.

- *Characterization of downlink coverage, area spectral efficiency and energy efficiency:* We also develop a tractable coverage probability model for an arbitrary UE at a desired SINR threshold. Our analysis accounts for both channel and spatial variations within the mmWave UE-centric S-cell model. The coverage probability is employed to quantify the area spectral efficiency of the system. We also analyze the performance of our proposed model in terms of the network wide energy efficiency.

- *Improved user quality of experience:* It is universally accepted that the bottleneck in wireless network performance is the cell edge performance degradation. The proposed architecture removes this problem and provides ubiquitous service to UEs. We investigate the SINR gains numerically through extensive Monte Carlo simulations under different UE service probabilities, RRH deployment densities and RRH (and UE) transmission beamwidths. Simulation results exhibit significant QoS enhancement for all UEs regardless of their location. The SINR gains stem from the independence of the distance between a UE and

its closest angularly interfering RRH from the RRH deployment density.

- *ASE and EE analysis:* We employ the developed analytical framework to investigate a key design question in practical deployment of proposed architecture, i.e. how do ASE and EE scale with the orchestration parameters, namely: 1) active UE population, 2) Stienen cell size coefficient, and 3) mmWave RRH deployment density? The answers are investigated for both single tier (DL via mmWave RRHs only) and multi-tier networks. Results show the variable level of sensitivity of the performance to our design parameters. We also observe conflicting trends of ASE and EE with certain design parameters, for instance, higher RRH density increases the network ASE but decreases the overall EE. This tradeoff can be modeled via a self-organizing network (SON) which fluctuates the network's operating state between the ASE-optimal and EE-optimal operating modes.
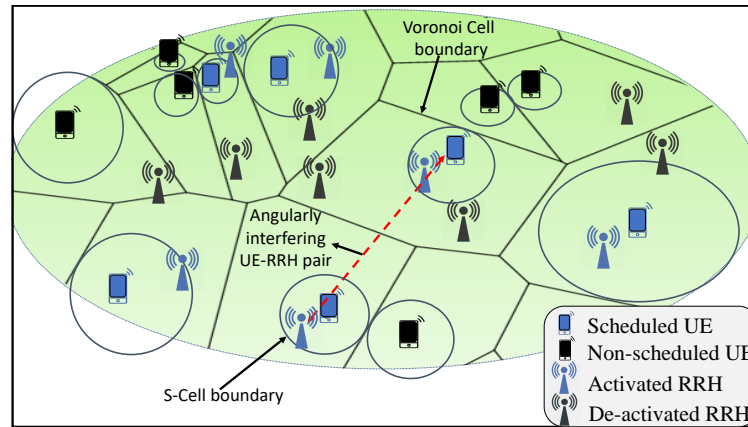

Fig. 1: The UE-centric S-cell architecture. The Voronoi tessellation of the plane is formed by Φ_{UE}. The circles around UEs represent S-cell edges at $\zeta = 1/2$. S-cell boundaries are not drawn to scale.

Paper Organization: In section II, we present system model for the proposed architecture and the UE-RRH association mechanism therein. Section III presents characterization of the distance distribution between a UE and its nearby angularly interfering RRHs. We continue with the quantification of the SINR coverage probability and the ASE for a single tier UE-centric S-cell network in section IV. Taking into account the practical deployment implication and requirement of a multi-tier set up, we present the SINR coverage probability and ASE in the multi-tier deployment scenario in section V. Section VI discusses the power consumption models for both MBS and RRH tiers and quantifies the overall energy efficiency of the proposed network model. Numerical results to validate the analytical framework and evaluate network wide efficiency of the proposed architecture in comparison to existing state-of-art network designs are presented in section VII. Conclusion and future research directions are presented in section VIII.

II. NETWORK MODEL

A. Spatial Model

We consider the downlink of a two-tier ultra-dense network consisting of one sub-6 GHz MBS that has mmWave RRHs and UEs spatially distributed across its foot-prints. Both the RRHs and UEs are assumed to be outdoors. This is to limit number of parameters in our model for simplicity. For indoor users, building penetration losses can be accounted for by appropriate scaling of the signal and interference powers. The spatial distributions for RRHs and UEs are modelled using two independent homogeneous Poisson point processes (HPPPs) Φ_{RRH} and Φ_{UE} with intensities λ_{RRH} and λ_{UE} respectively. The UE locations act as generating points for the UE-centric Voronoi tessellation. Each RRH is associated to a UE based on its physical location on the Voronoi plane. This implies that each RRH can at the most serve a single UE which is spatially closest to the RRH during a transmission time interval (TTI).

B. User-Centric Stienen Cell Geometry

To visualize a Stienen based user-centric cell design, consider the UEs as generating points of a 2-dimensional Poisson-Voronoi Tessellation. Every point in the convex polygons generated by the UEs is closer to its generating UE than to any other. Now a UE-centric Stienen cell can be formed by constructing around each UE a circular disk with a radius that is less than or equal to half of the distance between the UE and its closest neighbor (see Fig. 1). The resulting S-cell regions form a Poisson hard sphere model, which by definition is formed when the interiors of the disks centered at the generating points of the parent Poisson process do not overlap almost surely. The radius of the S-cell around a UE $u_j \in \Phi_{\text{UE}}$ is given as:

$$R_j = \min_{u_k} \zeta \parallel u_j - u_k \parallel; u_j, u_k \in \Phi_{\text{UE}}, j \neq k, \tag{1}$$

where $0 < \zeta \leq 1/2$ is the S-cell radius coefficient that models the flexibility in S-cell size. As $\zeta \to 0$, the S-cell size around UEs becomes negligible. For $\zeta = 0.5$, we obtain the largest possible S-cell sizes around each UE without overlap with adjacent S-cells. The coefficient provides control on modeling the S-cell sizes around UEs and is particularly useful in load balancing between RRHs and MBS in multi-tier networks. Note that $\zeta = 0.5$ creates the nearest neighbor model proposed by Stienen in [6].

We can observe from Fig. 1 that the user-centric Voronoi cells can be divided into two regions; the one within the circular Stienen cells and the other which is outside. This demarcation is particularly useful to ensure that as long as the serving RRH is within the Stienen cell, a UE

will not have any interfering RRH in a neighboring cell, that is spatially closer to the UE than its serving RRH.

C. Dual Slope LOS Ball Pathloss Model

Propagation in mmWave band in known to be severely impacted by blocking, atmospheric attenuation and low diffraction around obstacles. To effectively exhibit the blockage effects at high frequencies, a tri-state model is commonly used [15], according to which, a UE-RRH link can be in a line-of-sight (LOS), non-line-of-sight (NLOS) or outage state. A LOS link occurs when there is no blockage between a UE and its serving RRH. A NLOS link, on the other hand, occurs when the UE-serving RRH link is blocked, but the UE still receives sufficient signal strength through multipath components. An outage state refers to infinite pathloss, i.e., when the UE-RRH spatial separation is high enough to an extent that communication is not possible. The probability distribution for the tri-state model is based on experimental trials [7] and expressed as (2).

$$p_{\text{LOS}}(r) = \left[1 - \max\left(0, 1 - 181.27\exp(-r/30)\right)\right]\exp(-r/67.1),$$

$$p_{\text{NLOS}}(r) = \left[1 - \max\left(0, 1 - 181.27\exp(-r/30)\right)\right]\left(1 - \exp(-r/67.1)\right),$$

$$p_{\text{OUT}}(r) = 1 - p_{\text{LOS}}(r) - p_{\text{NLOS}}(r).$$

(2)

For analytical tractability, we use an equivalent LOS ball approximation where the pathloss is expressed as a Bernoulli random variable [16] with the assumption that all UE-RRH links are LOS within a distance constraint. If $p_{\text{LOS}}(r)$ and $p_{\text{NLOS}}(r)$ are the probabilities of a LOS and NLOS link between a UE and mmWave RRH at distance r respectively, then for the LOS ball radius of R_o,

$$p_{\text{LOS}}(r) = 1; \text{ if } r \leq R_o, \text{ and}$$

$$p_{\text{NLOS}}(r) = 1; \text{ if } r > R_o.$$

(3)

The described LOS ball model has been shown to simplify mathematical derivation in the system-level analysis at the cost of only a minor difference from the actual SINR distribution [17]. Although $p_{\text{LOS}}(r)$ for different UE-RRH links is not independent, it has been shown that the dependence is weak [18]; therefore we ignore potential blockage correlations in our model. Log-normal shadowing may be considered, but is not used to maintain the tractability of the model. From (3), the distinct pathloss behavior for LOS and NLOS links in our work is expressed as:

$$PL(r) = A_{\text{LOS}}r^{\alpha_{\text{LOS}}}; \text{ if } r \leq R_o, \text{ and}$$

$$= A_{\text{NLOS}}r^{\alpha_{\text{NLOS}}}; \text{ if } r > R_o,$$

(4)

where α_{LOS} and α_{NLOS} are the terrain and operating frequency dependent pathloss exponents for LOS and NLOS links respectively. The intercepts A_{LOS} and A_{NLOS} may be assumed identical if same closed-in reference distance is employed [19]. Note that high α_{NLOS} values result in sufficiently large $PL(r)$, effectively causing the UE-RRH links to be in outage as r increases.

D. UE-RRH Association Mechanism in a S-cell

A typical UE is associated to an RRH within its S-cell using the smallest path loss criteria. The smallest $PL(r)$ criteria ensures the maximum average SINR to each of the scheduled UEs. To cater for system limitations and interference management, we introduce a UE selectivity parameter $p_{\text{UE}} \in (0, 1]$ that is a random thinning factor denoting the percentage of UEs that will be considered for DL service in a given TTI. Here, $p_{\text{UE}} = 1$ implies that all the UEs that have at least one RRH in their S-cell will be scheduled for DL. Consequently, the served UEs form a thinned PPP $\Phi_{\text{UE}}^{\text{EF}}$ characterized by an intensity that is a function of p_{UE} as well as the RRH and UE densities and given by

$$\lambda_{\text{UE}}^{\text{EF}} = p_{\text{UE}}(1 - p_{\text{emp}})\lambda_{\text{UE}}, \tag{5}$$

where p_{emp} is the probability that a S-cell has no RRH to serve the associated UE. To evaluate the empty S-cell probability, we first express the probability density function (pdf) of the number of RRHs within the S-cell of a UE (see Lemma 2 in [14]) as

$$f_{n_{\text{RRH}}}(n_{\text{RRH}}) = \frac{\lambda_{\text{UE}}\zeta^{-2}}{\lambda_{\text{UE}}\zeta^{-2} + \lambda_{\text{RRH}}} \left(\frac{\lambda_{\text{RRH}}}{\lambda_{\text{RRH}} + \lambda_{\text{UE}}\zeta^{-2}} \right)^{n_{\text{RRH}}}. \tag{6}$$

The empty S-cell probability can simply be calculated by putting $n_{\text{RRH}} = 0$ in (6), i.e.

$$p_{\text{emp}} = \frac{\lambda_{\text{UE}}\zeta^{-2}}{\lambda_{\text{UE}}\zeta^{-2} + \lambda_{\text{RRH}}}. \tag{7}$$

To illustrate the effect of variable S-cell sizes, Fig. 2 shows the circular areas around UEs with different ζ values. As ζ increases, the number of RRHs within S-cells also increases, thereby increasing the intensity of the PPP representing interfering RRHs. This user scheduling scheme within the user-centric S-cell architecture is summarized as algorithm 1. Here, $b(\mathbf{x}, r)$ denotes a ball of radius r centered at a point $\mathbf{x}$.

From the practical implementation perspective, in the event of a RRH-free S-cell, user clustering strategies [20] may be employed where nearby UEs are grouped together and optimization is performed on the UE clusters rather than individual UEs. Such strategies are beyond the scope of this work and can be a topic of future extensions of this work.

E. mmWave Beamforming

It is assumed that both the UEs and RRHs are equipped with antenna arrays to perform directional beamforming. We assume a sectorized antenna gain pattern to allow for constant array gains within the main lobe and side lobe. A uniform planar array is considered at the mmWave RRH to enable beam steering in the azimuth as well as vertical plane. The number of elements and the inter-element distance can be varied to produce highly directional sectorized beam pattern in the desired direction. Since our model is based on single stream downlink communication,
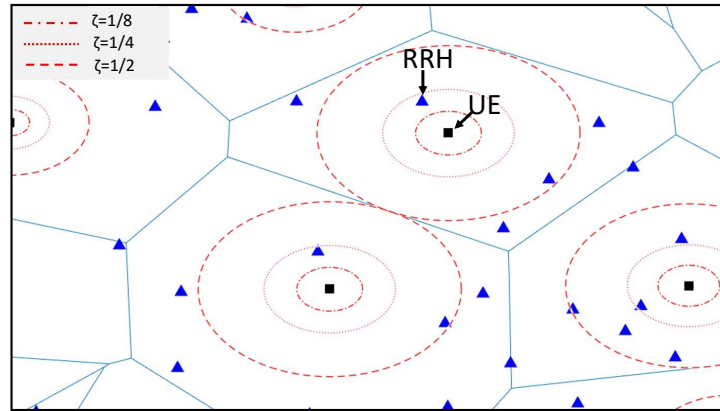
Fig. 2: The UE-centric Stienen cell sizes with different ζ values.

we prefer phased-array analog beamforming due to its simple design and ability to perform precoding in the RF domain. We also consider perfect channel knowledge between a UE and its serving RRH which enables them to adjust their beam steering orientation to achieve maximum directionality gain. For the sake of simplicity, we do not consider errors in channel estimation and synchronization (time and/or frequency) in the analytical framework. This assumption is reasonable due to beamforming in mmWave, which allows the UEs to be served in the high SNR regime. The mean square error in channel estimation at high SNR approaches 0 [21], therefore, we may neglect the channel estimation error in our model. Given $\mathrm{M} \in \{\mathrm{UE}, \mathrm{RRH}\}$, let G_{M}, g_{M} and θ_{M} denote the main lobe gains, side lobe gains and half power beamwidths (HPBWs) respectively of the UEs and RRHs. Then the directivity gain for a desired UE-RRH link is $G_{\mathrm{UE}}G_{\mathrm{RRH}}$. Assuming that the angle of arrival of an interfering beam at a typical UE is independent and uniformly distributed between $(0, 2\pi]$, the directivity gain G_{I} is a discrete random variable with the probability distribution given in [16] and mean interference gain for an arbitrary UE expressed as:

$$\mathbb{E}(G_{\mathrm{I}}) = \frac{\theta_{\mathrm{UE}}\theta_{\mathrm{RRH}}}{4\pi^2}G_{\mathrm{UE}}G_{\mathrm{RRH}} + \frac{\theta_{\mathrm{UE}}}{2\pi}\frac{1-\theta_{\mathrm{RRH}}}{2\pi}G_{\mathrm{UE}}g_{\mathrm{RRH}} + \frac{1-\theta_{\mathrm{UE}}}{2\pi}\frac{\theta_{\mathrm{RRH}}}{2\pi}g_{\mathrm{UE}}G_{\mathrm{RRH}} + \frac{(1-\theta_{\mathrm{UE}})(1-\theta_{\mathrm{RRH}})}{4\pi^2}g_{\mathrm{UE}}g_{\mathrm{RRH}}.$$

(8)

F. Channel Model

Due to the limited scattering behavior of mmWave signals, the Rayleigh fading model commonly used for sub-6 GHz band is not applicable [19]. Therefore, we assume independent Nakagami fading for each UE-RRH link with N_{L} and N_{N} representing the LOS and NLOS parameters respectively. The small-scale fading in signal power given by $|h|$ under the Nakagami assumption is a normalized Gamma random variable. We assume N_{L} and N_{N} to be positive integers. Furthermore, shadowing is not assumed for the sake of tractability.

Algorithm 1 UE scheduling algorithm in a user-centric S-cell network

---

Inputs: Φ_{RRH}, Φ_{UE}, p_{UE}, ζ

Outputs: Φ'_{RRH}, Φ'_{UE}

1: Initialize the set of scheduled UEs and the RRHs serving within the user-centric S-cells at any given time slot as Φ'_{UE}, $\Phi'_{\text{RRH}} \leftarrow \emptyset$.

2: Update $\Phi^{\text{EF}}_{\text{UE}}$ by thinning Φ_{UE} with a factor of p_{UE}.

3: For each $\boldsymbol{x} \in \Phi^{\text{EF}}_{\text{UE}}$, estimate the size of S-cell as $R_{\boldsymbol{x}} = \zeta d_{\boldsymbol{x}}$, where $d_{\boldsymbol{x}}$ is the distance to the nearest UE in $\Phi^{\text{EF}}_{\text{UE}}$.

4: Update Φ'_{RRH} and Φ'_{UE} for the current time slot using the following conditions:

foreach $\boldsymbol{x} \in \Phi^{EF}_{UE}$ **do**

    if $\boldsymbol{x} \cap b(\boldsymbol{x}, R_{\boldsymbol{x}}) \neq \emptyset$, $\forall \boldsymbol{x} \in \Phi^{EF}_{UE}$ **then**

        $\Phi'_{\text{UE}} \cup \{\boldsymbol{x}\}$

        foreach $\boldsymbol{y} \in \Phi_{RRH}$ **do**

            if $\boldsymbol{y} \in b(\boldsymbol{x}, R_{\boldsymbol{x}})$ **then**

                if $PL_{\boldsymbol{x},\boldsymbol{y}} < PL_{\boldsymbol{x},\boldsymbol{y'}}, \forall \boldsymbol{y'} \in \Phi_{RRH}, \boldsymbol{y'} \in b(\boldsymbol{x}, R_{\boldsymbol{x}}), \boldsymbol{y'} \neq \boldsymbol{y}$ **then**

                   $\Phi'_{\text{RRH}} \cup \{\boldsymbol{y}\}$

                end

            end

        end

    else

        continue.

    end

end

5: Serve all the scheduled users Φ'_{UE} from the associated RRHs in Φ'_{RRH}.

6: Go to step 1.

III. DISTANCE DISTRIBUTION TO ANGULARLY INTERFERING RRHs

In this section, we characterize the distribution of the distance between a typical UE scheduled on DL and the activated RRHs outside the UE's S-cell that have completely aligned antenna beams with the UE's directional beam. As discussed in section II-E, the probability of such an event occurring is $\frac{\theta_{\text{UE}}\theta_{\text{RRH}}}{4\pi^2}$. We focus on the angularly interfering RRHs, also called "angular interferers", because they contribute the largest share of interference at an arbitrary UE due to

maximum directivity gain. Exploiting the well-known fact that the distance between the nearest neighbors in a 2-D Poisson process is Rayleigh distributed [22], we can write the distribution of the distance between an arbitrary UE and its serving RRH given as r_o in Fig. 1 as:

$$f_{r_o}(r) = 2\pi r p_{\mathrm{UE}}\lambda_{\mathrm{UE}} \exp(-\pi r^2 p_{\mathrm{UE}}\lambda_{\mathrm{UE}}). \tag{9}$$

The tight packing in a Voronoi cell structure, especially in user hotspots, will inevitably give rise to scenarios with interfering RRHs co-located in close vicinity to the serving RRH. However, the requirement for narrow beam directionality in mmWave systems reduces the chances of exact alignment between a UE and an interfering RRH. Additionally, inherent to the Voronoi cell design, a UE-angularly interfering RRH pair must lie on opposite sides of the RRH serving that UE. This induces a mean minimum repulsion distance between a UE and an angularly interfering RRH which is equivalent to $\mathbb{E}(f_{r_o}(r))$.

Proposition 1: The distribution of the distance between a typical UE and its ith nearest angular interferer in a UE-centric S-cell network can be characterized as

$$f_{r_i}(r) = (r^{2i-1}) \left(\frac{p_{\mathrm{UE}}\lambda_{\mathrm{UE}}(1-p_{\mathrm{emp}})\theta_{\mathrm{UE}}\theta_{\mathrm{RRH}}}{4\pi} \right)^i \frac{2}{\Gamma(i)} \exp\left(\frac{-r^2 p_{\mathrm{UE}}\lambda_{\mathrm{UE}}(1-p_{\mathrm{emp}})\theta_{\mathrm{UE}}\theta_{\mathrm{RRH}}}{4\pi} \right). \tag{10}$$

Proof: See Appendix A. $\square$

Eq. (10) is obtained from the distribution of distance to the nth neighbor in a homogeneous Poisson point process [23]. Now the question is how the mean intensity of the PPP of the angularly interfering RRHs should be calculated.. Mathematically, it is calculated by the product of intensity of the PPP representing interfering RRHs and percentage of interfering links with completely aligned beams, given as $(p_{\mathrm{UE}}\lambda_{\mathrm{UE}}(1-p_{\mathrm{emp}})) * (\theta_{\mathrm{UE}}\theta_{\mathrm{RRH}}/(2\pi)^2)$.

IV. QUANTIFYING THE COVERAGE PROBABILITY AND AREA SPECTRAL EFFICIENCY IN A UE-CENTRIC S-CELL

Now that we have discussed the distance distribution of the angular interferers, we will proceed towards characterization of the coverage probability of a UE within a UE-centric S-cell design. Consider a scheduled UE $\mathbf{x} \in \Pi_{\mathrm{UE}}$. Let $\mathbf{o} \in (\Pi_{\mathrm{RRH}} \cap S(\mathbf{x}))$ be the RRH that yields minimum pathloss and is selected for DL service within $\mathbf{x}$'s S-cell area "$S(\mathbf{x})$" which is mathematically given as $S(\mathbf{x}) = b(\mathbf{x}, R_{\mathbf{x}})$. We consider the aggregate interference from both the angularly and non-angularly interfering RRHs. We have already seen in Section III that the mean intensity of the PPP representing the interfering RRHs is given by $\lambda_{\mathrm{IRRH}} = \lambda_{\mathrm{UE}}(1-p_{\mathrm{emp}})$. Without loss of

generality, we use the Silvnyak's theorem [24] and focus our analysis on the arbitrary UE $\mathbf{x}$ assumed to be located at the origin. With this assumption, the downlink SINR is given as:

$$\text{SINR} = \frac{\max_{\boldsymbol{o} \in (\Pi_{\text{RRH}} \cap S(\mathbf{x}))} h_{\boldsymbol{o}} G_{\text{UE}} G_{\text{RRH}} PL(r_{\boldsymbol{o}})}{\sigma^2 + \sum_{\boldsymbol{i} \in \Pi_{\text{IRRH}}} h_{\boldsymbol{i}} \mathbb{E}(G_{\text{I}}) PL(r_{\boldsymbol{i}})}, \tag{11}$$

where $r_{\boldsymbol{o}}$ and $r_{\boldsymbol{i}}$ are the relative distances of UE $\mathbf{x}$ with its DL scheduled and interfering RRHs respectively. σ^2 is the variance of the additive white Gaussian noise (AWGN) at the UE front end.

Once the interference is characterized, we can approximate the link success probability which represents the percentage of users with adequate link channel quality with the connected RRHs for DL. We can represent the QoS demands represented numerically through an SINR threshold γ_{th}. In this case, the coverage probability while taking into account the distinct fading characteristics and pathloss behaviors of LOS and NLOS links and is given by Theorem I.

Theorem 1: The link coverage probability of an arbitrary UE served under the proposed user-centric S-cell design and a one-to-one UE-RRH association scheme can be expressed as

$$P_{cov}(\gamma_{th}) = \sum_{n=1}^{N_{\text{L}}} (-1)^{n+1} \binom{N_{\text{L}}}{n} \int_0^{R_o} \exp(\frac{-n\eta_{\text{L}}\gamma_{th}\sigma^2 r^{\alpha_{\text{LOS}}}}{G_{\text{UE}}G_{\text{RRH}}}) \exp(-I_{\text{LL}}(\gamma_{th}, r)) \exp(-I_{\text{LN}}(\gamma_{th}, r)) f_{r_o}(r) \mathrm{d}r$$

$$+ \sum_{n=1}^{N_{\text{N}}} (-1)^{n+1} \binom{N_{\text{N}}}{n} \int_{R_o}^{\infty} \exp(\frac{-n\eta_{\text{N}}\gamma_{th}\sigma^2 r^{\alpha_{\text{NLOS}}}}{G_{\text{UE}}G_{\text{RRH}}}) \exp(-I_{\text{NL}}(\gamma_{th}, r)) \exp(-I_{\text{NN}}(\gamma_{th}, r)) f_{r_o}(r) \mathrm{d}r. \tag{12}$$

The terms I_{LL}, I_{LN}, I_{NL} and I_{NN} in (12) can be evaluated from equations (13)-(16).

$$I_{\text{LL}}(\gamma_{th}, r) = 2\pi\lambda_{\text{IRRH}} \sum_{k=1}^4 b_k \int_r^{R_o} F\left(N_{\text{L}}, \frac{n\eta_{\text{L}}\bar{a}_k\gamma_{th}r^{\alpha_{\text{LOS}}}}{N_{\text{L}}t^{\alpha_{\text{LOS}}}}\right) t\mathrm{d}t. \tag{13}$$

$$I_{\text{LN}}(\gamma_{th}, r) = 2\pi\lambda_{\text{IRRH}} \sum_{k=1}^4 b_k \int_{R_o}^{\infty} F\left(N_{\text{N}}, \frac{n\eta_{\text{L}}\bar{a}_k\gamma_{th}r^{\alpha_{\text{LOS}}}}{N_{\text{N}}t^{\alpha_{\text{NLOS}}}}\right) t\mathrm{d}t. \tag{14}$$

$$I_{\text{NL}}(\gamma_{th}, r) = 0.^{[1]} \tag{15}$$

$$I_{\text{NN}}(\gamma_{th}, r) = 2\pi\lambda_{\text{IRRH}} \sum_{k=1}^4 b_k \int_r^{\infty} F\left(N_{\text{N}}, \frac{n\eta_{\text{N}}\bar{a}_k\gamma_{th}r^{\alpha_{\text{NLOS}}}}{N_{\text{N}}t^{\alpha_{\text{NLOS}}}}\right) t\mathrm{d}t. \tag{16}$$

The quantities $\bar{a}_k$, b_k, $F(N, x)$ and η_i used in equations (13)-(16) are given by equations (17)-(20) respectively.

$$\bar{a}_k = \left[\frac{G_{\text{UE}}G_{\text{RRH}}}{G_{\text{UE}}G_{\text{RRH}}}, \frac{G_{\text{UE}}g_{\text{RRH}}}{G_{\text{UE}}G_{\text{RRH}}}, \frac{g_{\text{UE}}G_{\text{RRH}}}{G_{\text{UE}}G_{\text{RRH}}}, \frac{g_{\text{UE}}g_{\text{RRH}}}{G_{\text{UE}}G_{\text{RRH}}}\right]. \tag{17}$$

$$b_k = [\frac{\theta_{\text{UE}}\theta_{\text{RRH}}}{(2\pi)^2}, \frac{\theta_{\text{UE}}}{2\pi}(1 - \frac{\theta_{\text{RRH}}}{2\pi}),$$

$$(1 - \frac{\theta_{\text{UE}}}{2\pi})\frac{\theta_{\text{RRH}}}{2\pi}, (1 - \frac{\theta_{\text{UE}}}{2\pi})(1 - \frac{\theta_{\text{RRH}}}{2\pi})]. \tag{18}$$

---

[1]This is a direct consequence of the Ball LOS approximation model according to which if a UE is being served by an RRH in NLOS region (i.e. $r_o > R_o$), no interfering RRH will have a LOS link with that UE.

$$F(N, x) = 1 - \frac{1}{(1+x)^N}. \tag{19}$$

$$\eta_i = N_i(N_i!)^{-\frac{1}{N_i}}. \tag{20}$$

Proof: See Appendix B.

$\square$

Eq. (12) is a consequence of the independence of the PPPs representing LOS and NLOS interferers. The Laplace functional of each PPP yields 2 terms: one when the serving RRH is within the LOS region and other when the serving RRH is in the NLOS region. The term I_{LL} is for the scenario when both the serving RRH and interfering RRH are within the LOS region. The term I_{LN} is for the scenario when the serving RRH is the LOS region but the interfering RRH in the NLOS region. The term I_{NL} is for the unlikely scenario when the serving RRH is in the NLOS region while the interfering RRH is in the LOS region. Therefore, the value of this component is 0. Finally, the term I_{NN} is for the event when both the serving and interfering RRHs are in the NLOS region.

The system-wide area spectral efficiency is measured as the number of bits which can be transmitted per Hertz bandwidth per second within 1 squared meter area. We discuss the ASE for two different DL transmission mechanisms:

1) Fixed Rate Transmission: In a fixed rate transmission, all UEs which meet the SINR criteria for DL transmission are scheduled with uniform data rate links. The potential throughput for a UE-centric S-cell architecture in this scenario can be quantified as

$$\mathrm{ASE}_{\mathrm{FR}} = \lambda_{\mathrm{UE}}^{\mathrm{EF}} \log_2(1 + \gamma_{th}) P_{cov}(\gamma_{th}). \tag{21}$$

2) Adaptive Rate Transmission: In this system, each UE is provided a DL data rate which is proportional to its SINR, subject to meeting the SINR threshold criteria. Mathematically, the ASE in this situation may be expressed as

$$\mathrm{ASE}_{\mathrm{AR}} = \frac{1}{\mathbb{A}} \sum_{u \in \Phi_{\mathrm{UE}}^{\mathrm{EF}}} \log_2(1 + \mathrm{SINR}_u); \text{ if } \mathrm{SINR}_u > \gamma_{th}, \tag{22}$$

where $\mathbb{A}$ is the total network area under consideration. As is clear from (21) and (22), the area spectral efficiency of the UE-centric S-cell is strongly coupled with p_{UE}. Intuitively, a higher p_{UE} increases the effective number of scheduled users. However it also lowers the SINR due to shorter mean distance of a UE to its closest interfering RRH. In the results section, through evaluation of the attainable area spectral efficiency, we will investigate which of the two opposite effects is dominant in the proposed architecture.

V. UE-Centric S-cell Architecture in a Multi-tier Network

Until now, we have analyzed how a UE-centric Stienen cell architecture is modeled for a single tier network where UEs are only served if there resides at least one mmWave RRH within its S-cell area as depicted in Algorithm 1. Needless to point out, this gives rise to longer wait times and even results in network outage (due to larger UE-serving RRH distance) in sparse RRH deployment regions. It is therefore pertinent to include the analysis of a multi-tier system with MBS tier serving the UEs which do not have any RRH within their S-cell at sub-6 GHz. There is a two-fold advantage of this approach: firstly, operating the MBS and RRH tier in different frequency bands avoids any co-tier interference, and secondly, it is well known that propagation loss on sub-6 GHz band is less severe as compared to mmWave, allowing MBS to serve UEs at larger distances. With respect to UE association, the mechanism will have slight modifications as compared to Algorithm 1. All the UEs that are void of RRHs within their S-cell are connected to their respective MBS for DL coverage. Let us consider that Φ_{MBS} and $\Phi_{\mathrm{UE,MBS}}$ are PPPs, with mean intensities λ_{MBS} and $\lambda_{\mathrm{UE,MBS}}$ respectively, and represent MBS deployment density and UEs served by MBSs respectively. Unlike RRH deployment which is impromptu and hence is modelled well by PPP, MBS deployment is likely to be well planned. Therefore, to model realistic MBS deployment, we induce repulsion between the PPP representation of MBS tier. This is done by modeling it as a type II Matern hardcore process [24] where we choose a subset of the original PPP with a distance constraint. Mathematically, the thinned PPP representation of MBS is given by

$$\lambda_{\mathrm{MBS}}^{\mathrm{EF}} = \frac{1 - \exp(-4\pi\lambda_{\mathrm{MBS}} R_{\mathrm{MBS}}^2)}{4\pi R_{\mathrm{MBS}}^2}. \tag{23}$$

(23) implies that the minimum allowable distance between adjacent MBSs is $2R_{\mathrm{MBS}}$. The analytical characterization of network level KPIs for the proposed UE-centric S-cell under the multi-tier network is presented below:

A. SINR

The SINR at a UE $\mathbf{x}$ connected to a RRH or MBS is dependent on the presence of an RRH within its S-cell and is given by a piece-wise function in (24). For the UEs connected to MBSs, we consider Rayleigh fading environment. This implies that when $\boldsymbol{x} \in \Phi_{\mathrm{UE,MBS}}$, the channel gain ($h_o$ and h_i) is assumed to be a unit mean exponential random variable and path loss at $\mathbf{x}$ from an RRH $\mathbf{y}$ is modeled by $l(||\boldsymbol{x} - \boldsymbol{y}||) = ||\boldsymbol{x} - \boldsymbol{y}||^{-\alpha_{\mathrm{MBS}}}$ power-law function.

$$\mathrm{SINR}_{\mathrm{MT}} = \begin{cases} \frac{\max_{\boldsymbol{o} \in \Pi_{\mathrm{RRH}} \cap S(\mathbf{x})} h_{\boldsymbol{o}} G_{\mathrm{UE}} G_{\mathrm{RRH}} PL(r_{\boldsymbol{o}})}{\sigma^2 + \sum_{i \in \Pi_{\mathrm{IRRH}}} h_{\boldsymbol{i}} \mathbb{E}(G_1) PL(r_{\boldsymbol{i}})} & \boldsymbol{x} \in \Phi_{\mathrm{UE}}' \\ \frac{\max_{\boldsymbol{o} \in \Pi_{\mathrm{MBS}}} h_{\boldsymbol{o}} PL(r_{\boldsymbol{o}})}{\sigma^2 + \sum_{i \in \Pi_{\mathrm{MBS}'}} h_{\boldsymbol{i}} PL(r_{\boldsymbol{i}})} & \boldsymbol{x} \in \Phi_{\mathrm{UE,MBS}} \end{cases} \tag{24}$$

B. Coverage Probability

For a multi-tier network, the coverage probability is dependent on both the SINR threshold γ_{th} and the probability of a UE being served by an RRH, which is a function of ζ and p_{emp}. Mathematically, the coverage probability is given by

$$P_{cov,\text{MT}}(\gamma_{th}) = (1 - p_{\text{emp}})P_{cov}(\gamma_{th}) + p_{\text{emp}}P_{cov,\text{MBS}}(\gamma_{th}), \tag{25}$$

where $P_{cov}(\gamma_{th})$ is the coverage probability of a UE connected to a mmWave RRH given by (12) while $P_{cov,\text{MBS}}(\gamma_{th})$ is the probability that the SINR at an arbitrary UE served by an MBS exceeds the QoS threshold, i.e. SINR $\geq \gamma_{th}$. The coverage probability $P_{cov,\text{MBS}}(\gamma_{th})$ is inspired from the work in [22] for the Rayleigh fading scenario and expressed as

$$P_{cov,\text{MBS}}(\gamma_{th}) = \pi\lambda_{\text{MBS}} \int_0^\infty \exp\left(-\pi\lambda_{\text{MBS}}r\left[1 + \gamma_{th}^{2/\alpha_{\text{MBS}}}\int_{\gamma_{th}^{-2/\alpha_{\text{MBS}}}}^\infty \frac{1}{1 + v^{\alpha_{\text{MBS}}/2}}dv\right] - \gamma_{th}\sigma^2 r^{\alpha_{\text{MBS}}/2}\right) dr, \tag{26}$$

where α_{MBS} is the pathloss exponent for the propagation on MBS tier.

C. Area Spectral Efficiency

In the same spirit as Section IV, the area spectral efficiency for a multi-tier network can be evaluated for fixed rate and adaptive rate transmissions as (27) and (28) respectively:

$$\text{ASE}_{\text{FR,MT}} = \lambda_{\text{UE}}p_{\text{UE}}\log_2(1 + \gamma_{th})[(1 - p_{\text{emp}})P_{cov}(\gamma_{th}) + p_{\text{emp}}P_{cov,\text{MBS}}(\gamma_{th})]. \tag{27}$$

$$\text{ASE}_{\text{AR,MT}} = \frac{1}{\mathbb{A}}\left[\sum_{u\in\Phi_{\text{UE}}^{\text{EF}}}\log_2(1 + \text{SINR}_u) + \sum_{v\in\Phi_{\text{UE,MBS}}}\log_2(1 + \text{SINR}_v)\right], \tag{28}$$

where SINR_u and SINR_v are the SINR quantities for RRH and MBS connected UEs respectively and given by (24).

VI. ENERGY EFFICIENCY ANALYSIS

The power consumption of a stand-alone small cell RRH is investigated in the project EARTH [25]. This model was extended further to integrate the benefits of centralized processing in [26]. Taking inspiration from these works, we formulate the power consumption for both the MBSs and small cell RRHs as a linear combination of fixed power and load dependent power consumption components. Mathematically, the total power consumption of the two-tier network can be simplified as

$$P = |\mathbb{A}|\{\underbrace{\lambda_{\text{MBS}}^{\text{EF}}\left(A_{\text{MBS}}P_{\text{MBS,Tx}} + B_{\text{MBS}}\right)}_{\textbf{MBS-Tier Power}} + \underbrace{\lambda_{\text{UE}}p_{\text{UE}}(1 - p_{\text{emp}})P_{cov}(\gamma_{th})\left(A_{\text{RRH}}P_{\text{RRH,Tx}} + B_{\text{RRH}}\right)}_{\textbf{Activated RRH-Tier Power}}$$
$$+ \underbrace{B_{\text{RRH}}\left(\lambda_{\text{RRH}} - \lambda_{\text{UE}}p_{\text{UE}}(1 - p_{\text{emp}})P_{cov}(\gamma_{th})\right)}_{\textbf{De-activated RRH-Tier Power}}\}. \tag{29}$$

B_{MBS} (and B_{RRH}) denotes the fixed power consumption of an MBS (and RRH). This is the energy cost which is bore by the network regardless of the number of UEs requesting DL service. The coefficients A_{MBS} (and A_{RRH}) lump together frequency dependent response of a power amplifier and several other factors within MBS (and RRH). The coefficients A_i and B_i, where $i \in \{\text{MBS,RRH}\}$ are expressed as

$$A_i = \frac{1}{\eta_i^{\text{PA}}(1 - \sigma_i^{\text{feed}})(1 - \sigma_i^{\text{MS}})(1 - \sigma_i^{\text{DC}})(1 - \sigma_i^{\text{cool}})}, \text{ and} \tag{30}$$

$$B_i = \frac{P_{i,\text{RF}} + P_{i,\text{BB}}}{(1 - \sigma_i^{\text{MS}})(1 - \sigma_i^{\text{DC}})(1 - \sigma_i^{\text{cool}})}. \tag{31}$$

Note that we are considering an always ON MBS deployment to avoid coverage holes and provide uninterrupted control/signaling to the UEs. The power saving in the proposed architecture will thus come from intelligently turning OFF mmWave RRHs that are not providing DL data services to UEs. For detailed explanation of the power consumption parameters, readers are referred to [25]. The network wide EE is analyzed for adaptive rate transmission scenario in our work and expressed mathematically as

$$EE = \frac{\mathbb{A}[\text{ASE}_{\text{AR,MT}}]}{P}. \tag{32}$$

EARTH's segmentation of the power consumption employed in this work allows us to analyze the amount of energy saving possible when an RRH is turned OFF. It is well known that the major chunk of power consumption in a cellular BS takes place within the power amplifier. By dynamic shutting down of the power amplifier and the associated transmission unit, there is significant energy saving, especially in dense deployments. In the next section, we will look at the potential power saving in terms of EE variation with adjustments in three network parameters: i) served UE percentage, ii) RRH deployment density, and iii) user-centric S-cell sizes.

VII. RESULTS AND DISCUSSION

In this section, we present numerical as well as Monte Carlo simulation results to evaluate the validity of the developed model. After ensuring accuracy of the models, we compare the performance of single and mult-tier UE-centric S-cell architectures in mmWave networks with the conventional architecture. Our proposed network model analyzes the interplay of network performance measures that are relevant to 5G communication networks. These include area spectral efficiency, energy efficiency, and users' quality of experience. By choosing different design configurations, we will try to ascertain the circumstances in which our proposed model outperforms state-of-the-art architectures. For instance, if we have different spatio-temporal regions in a network coverage area with sparse and dense user distributions, our framework enables an operator to manage the tradeoff between ASE and EE with activation of appropriate number of mmWave RRHs. Additionally, we ascertain the scheduling delay induced by the model and the impact of channel estimation errors on the metric performance. Unless otherwise specified, the basic simulation parameters used in our analysis are given in Table 1.

TABLE I: SIMULATION PARAMETERS

Parameter	Value
Simulation area dimensions ($\|\mathbb{A}\|$)	100 m x 100 m
Mean PPP density: $\lambda_{UE}\|\mathbb{A}\|$; $\lambda_{RRH}\|\mathbb{A}\|$; $\lambda_{MBS}\|\mathbb{A}\|$	400;400;16
p_{UE}	[0.25 0.5 0.75 1]
$\theta_{UE}, \theta_{RRH}$	$[7^o \ 10.9^o]$
UE, RRH Antenna specifications: G_{UE}; G_{RRH};g_{UE}; g_{RRH}	10 dB; 10 dB; -3 dB; -3 dB;
R_o (from (2)); N_L; N_N	46.5 m; 3; 2
Pathloss exponents: α_{LOS}; α_{NLOS}; α_{MBS}	2.4; 4.7; 3
A_{LOS}, A_{NLOS}	1
R_{MBS}	50 m
$P_{MBS,Tx}$; $P_{RRH,Tx}$	10 W; 1 W
RRH Power Consumption parameters: $\eta^{PA}_{RRH},\sigma^{feed}_{RRH},\sigma^{MS}_{RRH},\sigma^{DC}_{RRH},\sigma^{cool}_{RRH}$,$P_{RRH,RF}$, $P_{RRH,BB}$	0.0025,0,0.1,0.08,0, 0.4 W,1.2 W
MBS Power Consumption parameters: $\eta^{PA}_{MBS},\sigma^{feed}_{MBS},\sigma^{MS}_{MBS},\sigma^{DC}_{MBS},\sigma^{cool}_{MBS}$,$P_{MBS,RF}$,$P_{MBS,BB}$	0.388,0,0.07,0.06,0.09, 10.9 W,14.8 W
A_{RRH}; B_{RRH}; A_{MBS}; B_{MBS} (based on power consumption parameters)	23.22; 1.932; 3.24; 32.3
No. of Monte Carlo realizations	100000

A. Model Validation

We validate the expression for SINR coverage probability derived in Theorem I in Fig. 3. The plot shows close agreement between the simulations and the derived analytical results, particularly at high γ_{th} regimes. We observe that the analytical model holds true for variations in both ζ (Fig. 3 (a)) and p_{UE} (Fig. 3 (b)), keeping the other parameter fixed. Fig. 3 also depicts a decrease in coverage probability at higher ζ and p_{UE} for the same SINR threshold. This is intuitive because a larger p_{UE} reduces the average UE-interfering RRH distance. As a consequence, the average interference increases which reduces the coverage probability of an arbitrary UE. Similarly, a larger ζ means larger S-cell area which increases the probability of a UE being served due to presence of at least one RRH within its S-cell (see Fig. 2). In other words, higher ζ results in greater number of activated RRHs which increases the overall interference for an arbitrary UE.

To validate the distance distribution of angularly interfering RRHs derived in section III, we compare the analytical and Monte Carlo simulation results for λ_{IRRH} in Fig. 4. Results show the formulated model to be quite accurate for variations in both p_{UE} and ζ for a range of RRH densities. Another interesting observation from Fig. 4. is the high sensitivity of interfering RRH density to ζ. Increasing ζ by 2 at $p_{UE} = 1$ yields an interfering RRH density increase of about
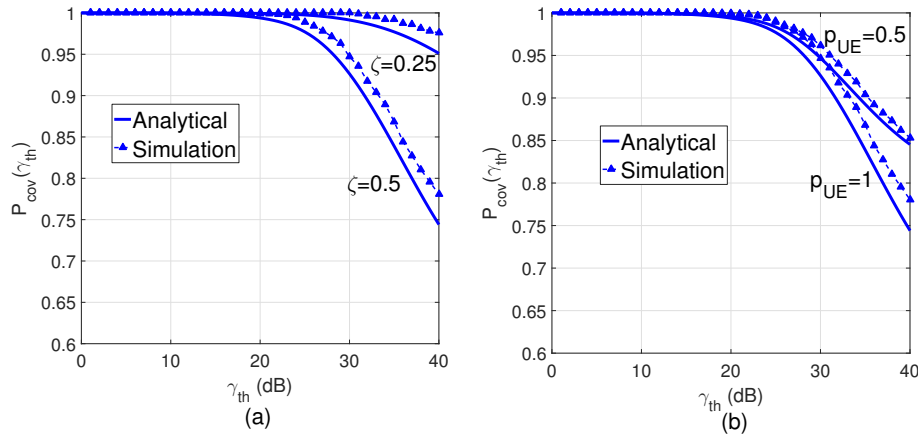
Fig. 3: SINR coverage probability at: (a) different ζ and p_{UE}=1, (b) different p_{UE} and $\zeta = 0.5$.
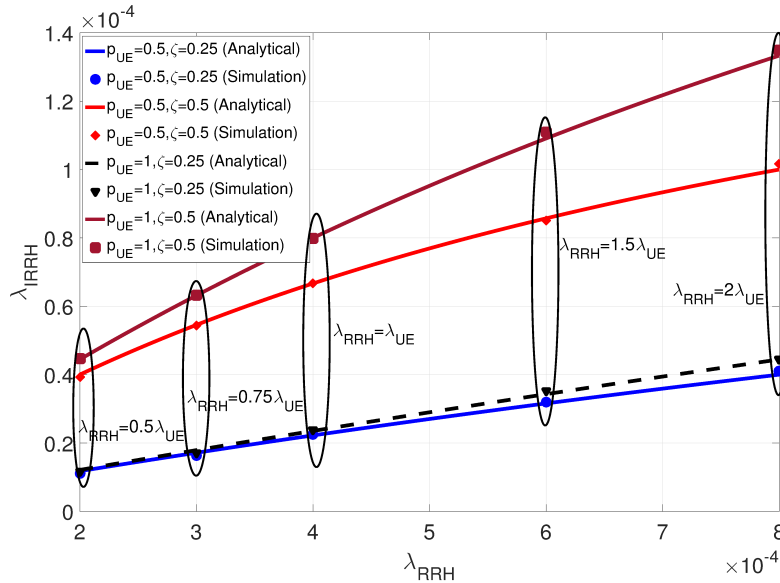

Fig. 4: Interfering RRH density validation at different ζ and p_{UE} values.

220% while the same increase in p_{UE} at $\zeta = 0.5$ yields only 35% increase in interfering RRHs.

B. Sensitivity Analysis

Next, we analyze the gradient of coverage probability with respect to UE selection probability and the S-cell size in Fig. 5. Keeping uniform intervals for the possible range of p_{UE} and ζ, we note that the rate of change of coverage probability is far more sensitive to an interval change in ζ. Negative gradient is observed for the entire range of p_{UE} and ζ which makes sense because an increase in either of these parameters results in a larger number of interfering RRHs and a subsequent reduction in coverage probability. The peak absolute value for $\frac{dP_{cov}}{dp_{UE}}$ and $\frac{dP_{cov}}{d\zeta}$ occur at $p_{UE} = 0.34$ and $\zeta = 0.35$ respectively. However, the rate of coverage change per interval variation
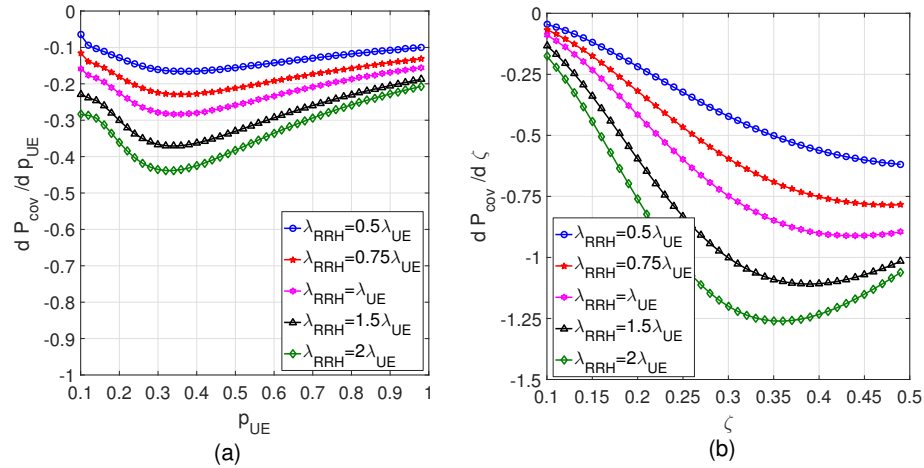
Fig. 5: Gradient of coverage probability with respect to: (a) p_{UE} and (b) ζ.
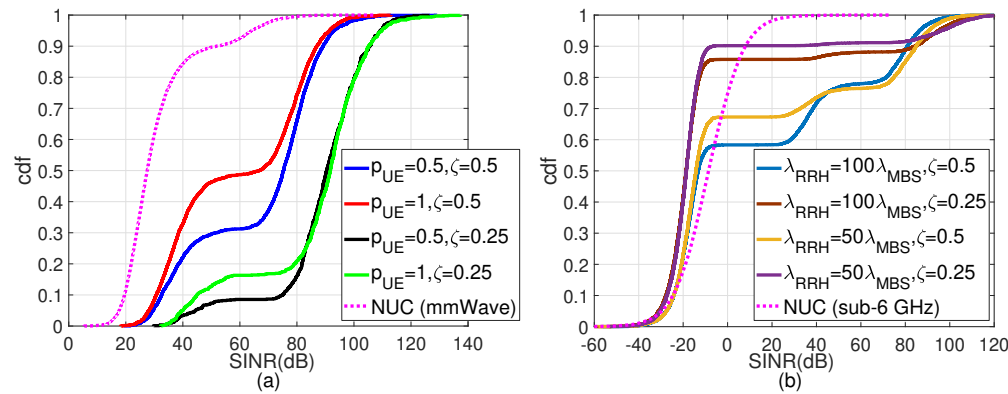

Fig. 6: Downlink SINR cdf comparison between user-centric S-cell and non user-centric approaches in (a) single-tier and (b) multi-tier networks.

in ζ is almost 3 times as compared to when p_{UE} is varied. This is in agreement with Fig. 4 which demonstrated higher increase in interfering RRHs with a unit increase in ζ. Both Figs. 5(a) and 5(b) demonstrate that the impact on coverage probability reduction is found to be less severe in sparse RRH deployments. The results provide design insights for the proposed UE-centric S-cell network, for instance, with regards to choosing between UE selection parameter adjustment and S-cell size adjustment or appropriate combination of the two for optimizing coverage.

C. QoE Enhancement in User-Centric S-cell Network

Users' QoE analysis is conducted through SINR distribution between UEs at different p_{UE} and ζ values in Fig. 6. To compare the QoE performance with a standard non user-centric PPP deployment, we follow the approach in [17] and represent it as "NUC". Results in Fig. 6 (a) for a single tier mmWave network show that the UE-centric S-cell approach yields an SINR
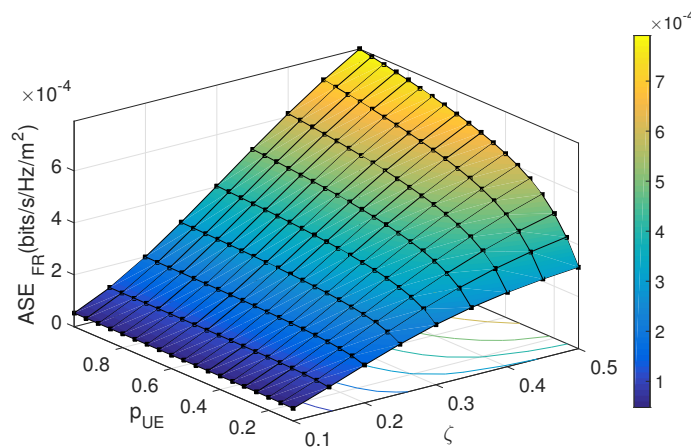
Fig. 7: ASE v/s p_{UE} and ζ in a UE-centric S-cell network

gain ranging from 40 dB to 65 dB for almost 50% of the users. Following the same trend from Figs. 4 and 5, the SINR observed a marked gain from a decrease in ζ. As discussed earlier, the increase in SINR at lower ζ values is a result of thinning of the PPP Π_{IRRH} and a consequent increase in the average interferer distance.

The multi-tier SINR cumulative distribution function (cdf) in Fig. 6 (b) shows some interesting trends. We observe a clear distinction between the SINR of the UEs connected to the MBS and mmWave RRH tiers. More specifically, three distinct regions can be identified from the multi-tier SINR distribution plot in Fig. 6(b): i) the majority of UEs having SINR less than -10 dB SINR for all the simulation cases; ii) a set of UEs with SINR between 25 dB and 50 dB for $\zeta = 0.5$; and iii) a set of UEs with SINR above 70 dB for $\zeta = 0.5$. These jumps of 35 dB and 20 dB are observed as we transition from sub-6 GHz MBS connected UEs to NLOS mmWave RRH connected UEs, and then from NLOS to LOS mmWave RRH connected UEs respectively. For the same S-cell size, a denser RRH deployment pushes more UEs to the RRH tier. Although the number of UEs connected to mmWave RRH tier increases, the resulting average SINR for the tier is lower as compared to a sparse RRH deployment due to a higher number of interfering mmWave RRHs. This allows the network operator to fluctuate the design parameters and choose between a small number of UEs connected to mmWave RRHs with extremely high user QoE or a larger number of UEs connected to mmWave RRHs with moderately lower QoE.

D. ASE, EE Performance in Single-tier User-Centric S-cell Networks

In this sub-section, we investigate the system wide ASE performance in fixed rate as well as adaptive rate transmission scenarios and the impact of p_{UE}, ζ, θ_{RRH} and λ_{RRH} on ASE. Results
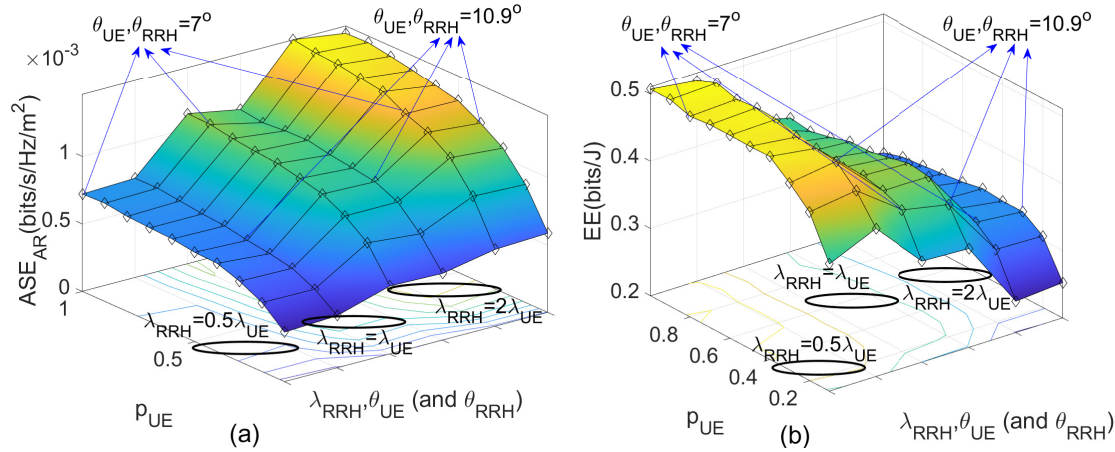
Fig. 8: ASE and EE variation with UE selection parameter, RRH densities and transmission beamwidths.

in Fig. 7 reveal that fixed rate ASE is a monotonically increasing function of both ζ and p_{UE}. This implies that the increase in $\lambda_{\text{UE}}^{\text{EF}}$ accompanied by a higher p_{UE} dominates the decrease in the SINR coverage probability observed in Fig. 3. Similar to the earlier presented results in Fig. 5, ASE_{FR} is more sensitive to ζ with the steepest gradient at $p_{\text{UE}} = 1$.

Fig. 8 presents the Monte Carlo simulation results for the adaptive rate area spectral efficiency and energy efficiency for the single tier UE-centric S-cell network. We observe a significant increase in the ASE (Fig. 8 (a)) as the density of RRH deployments increases. The overall trend for ASE with regards to p_{UE} is monotonic increase, with the increment being almost 46% as p_{UE} goes from 0.1 to 0.2. For $p_{\text{UE}} > 0.5$, we only observe a marginal gain in ASE upon further increments in p_{UE}, keeping all other network parameters constant. Additionally, we observe a marginal ASE reduction with wider antenna beamwidths as a result of higher λ_{AIRRH} when θ_{UE} (and / or) θ_{RRH} are increased. The network wide EE plotted as Fig. 8 (b) peaks on average for $0.4 \leq p_{\text{UE}} \leq 0.6$. As expected, the EE results show opposite trend for dense RRH deployments as a high number of activated mmWave RRHs contribute towards additional energy costs for the operator. There is no observable link between EE and the UE (and RRH) transmission beamwidths. We observe a slight increase in EE for wider beamwidths when $\lambda_{\text{RRH}} = \frac{1}{2}\lambda_{\text{UE}}$ and $\lambda_{\text{RRH}} = 2\lambda_{\text{UE}}$, but a decrease in the case of $\lambda_{\text{RRH}} = \lambda_{\text{UE}}$. From a network operator's perspective, the findings highlight the necessity of a SON implementation in order to determine the right balance between maximizing net throughput and minimizing cost per bit.
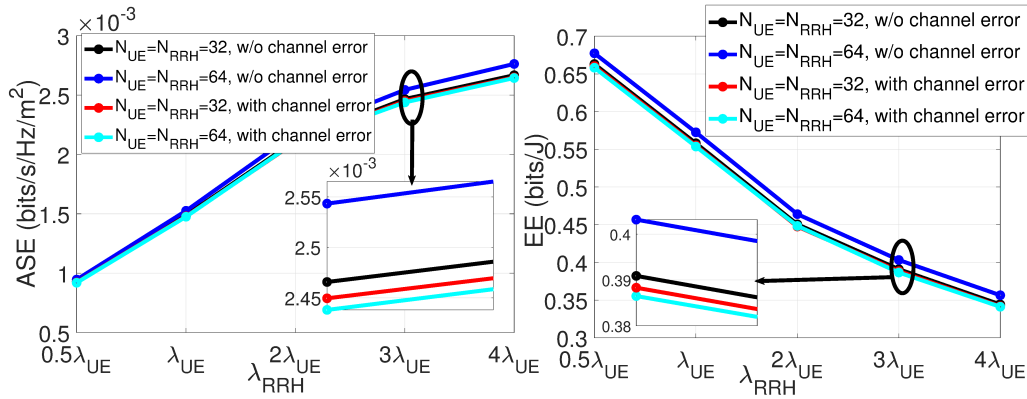
Fig. 9: Impact of channel estimation error and antenna array size on ASE and EE.

To study the impact of channel estimation errors and number of antenna elements on the arrays at the UE and mmWave RRH, we plot the ASE and EE for different configuration scenarios in Fig. 9. When complete channel state information is available at both the UE and RRH, we see that increasing the number of antenna elements improves the ASE and EE performance. This is simply due to the fact that a larger antenna array yields higher directionality gain, therefore the mean interference from concurrent transmissions reduces consequentially. For channel estimation errors, we follow the approach adopted in [27] and consider both SNR degradation as well as loss in directivity gain due to angle of destination (AoD) estimation errors. Considering Gaussian AoD estimation errors with a variance of 6° at the RRH and / or UE, we observe that both ASE and EE performance degradation is more pronounced when number of antennas at mmWave RRH (N_{RRH}) and UE (N_{UE}) are 64 instead of 32. Larger antenna array size corresponds to narrow propagation beams, and even a small AoD estimation inaccuracy in this case causes severe directionality gain degradation which reduces both ASE and EE.

E. Performance Comparison with Fixed Size User-Centric Networks

Fig. 10 shows the performance gains in terms of adaptive rate area spectral efficiency (Fig. 10(a)), energy efficiency (Fig. 10(b)) and mean UE scheduling ratio (Fig. 10(c)) for the proposed UE-centric S-cell architecture in comparison to the non-elastic fixed sized circular user-centric service regions proposed in earlier works [28]. The network models with fixed user-centric regions in [28] to maximize ASE and EE are referred to as FS(ASE) and FS(EE) respectively. The S-cell user-centric network used for comparison is configured at $p_{UE} = 1$ and $\zeta = \{0.25, 0.5\}$. Clearly, the proposed model at $\zeta = 0.5$ outperforms both extremes of the earlier "one-size fits all" strategy in terms of system throughout at dense mmWave RRH deployment scenarios at

the cost of marginal EE loss as compared to FS(ASE). The user-centric S-cell at $\zeta = 0.25$ exhibits higher efficiency than FS(EE) for all the three measures at $\lambda_{RRH} \geq 2\lambda_{UE}$. This is because denser deployments reduce empty S-cells and due to shorter UE-RRH spatial distance, higher throughput is achieved which increases both ASE and EE. In addition to higher aggregate throughput, Fig. 10(c) shows that the user-centric S-cell network also reduces mean waiting time for an arbitrary UE from 2.5 TTIs in FS(ASE) to 2 TTIs when $\zeta = 0.5$. This can be traced to the non-conflicting nature of the proposed user-centric S-cell design where all the UEs that have at least one mmWave RRH within their S-cell are scheduled on DL. On the other hand, scheduling success in the non-flexible user-centric model in [28] depends upon both the probability of cell overlap with nearby UEs and probability of presence of a serving mmWave RRH within the user-centric cell.
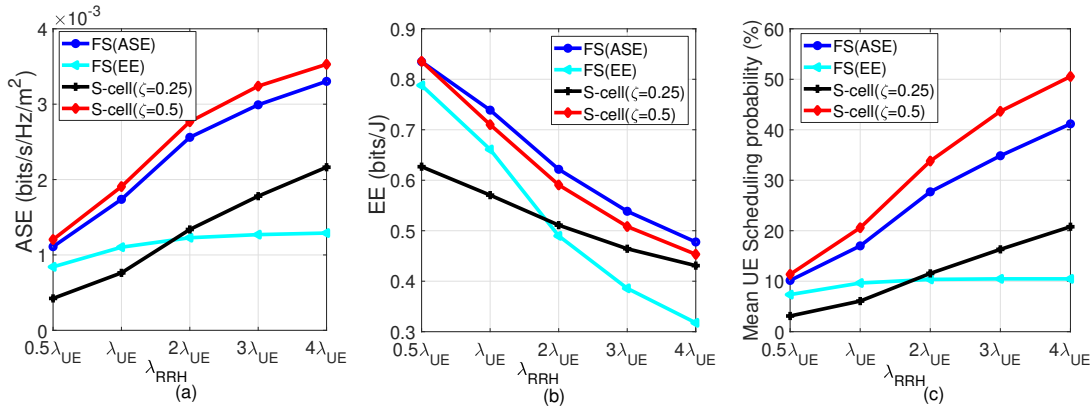

Fig. 10: (a) ASE, (b) EE and (c) UE scheduling ratio comparison of non-elastic user-centric [28] and proposed user-centric S-cell approaches under different RRH densities.

F. ASE, EE Performance in Multi-Tier User-Centric S-cell Networks

In Fig. 11, we compare the inter-tier load distribution for three different S-cell sizes at $\zeta = 1/8$, $\zeta = 1/4$ and $\zeta = 1/2$. $\zeta = 1/2$ yields the most proportionate UE distribution between the MBS and mmWave RRH tiers. Apparently, setting a high ζ value seems the most obvious choice for offloading a congested MBS-tier. This is because a higher ζ pushes a large number of UEs from the MBS to mmWave RRH tier. A large ζ value not only allows more UEs connected served by the RRH tier to avail the wider mmWave spectrum, but also reduces the average interference at a typical UE due to highly directional transmission in mmWave RRH tier as opposed to omni-directional transmission from interfering MBSs in the sub-6 GHz MBS tier.

To assess the uniformity in the achievable throughput amongst UEs, we apply the Jain's fairness equation [29] on the UE throughput in a given TTI. The Jain's fairness index (JFI) values
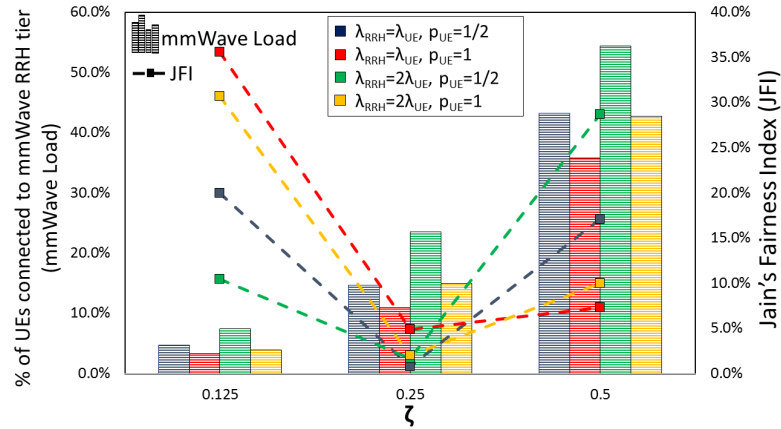
Fig. 11: UE load distribution between MBS and RRH tiers and achievable throughput fairness index in a two-tier user-centric S-cell network.

plotted in Fig. 11 exhibit highest values at $\zeta = 1/8$ when a large proportion of UEs is connected to the MBS tier. The JFI dips below 10 % for all the considered RRH deployment and p_{UE} scenarios at $\zeta = 1/4$ when the UEs in mmWave connectivity are mostly within LOS boundary due to smallness of the UE-centric S-cell regions. As a result, there is a large disproportion between SINRs of UEs connected to mmWave RRHs and sub-6 GHz MBS tier. Nevertheless, the fairness index improves at $\zeta = 1/2$ when the number of UEs connected to mmWave RRHs increases, particularly in the NLOS regions. Another interesting observation from the JFI results is that while a dense RRH deployment and sparse UE selection maximizes fairness at $\zeta = 1/2$, the vice versa exhibits highest fairness at $\zeta = 1/8$. This trend can be explained from the inter-tier UE distribution graph. The JFI is maximized (and UE throughput disparity is minimized) when we have the least mmWave load percentage at $\zeta = 1/8$. However, at $\zeta = 1/2$, higher mmWave tier percentage results in more UEs experiencing similar QoS, and hence increasing overall JFI.

Hitherto, we have seen how the network level ASE and EE behave with variations in the three adjustable network parameters, i) S-cell size (characterized via ζ), ii) UE selection probability (p_{UE}), and iii) mmWave RRH deployment density (λ_{RRH}). The question that begs further analysis is whether there is an optimal combination of these parameters which simultaneously maximizes the network wide ASE and EE. Fig. 12 plots the adaptive rate ASE and EE for the multi-tier user-centric S-cell network under variation, within practical range, of each parameter while keeping the other two constant. The overall trend for ASE is positive for increments in each of the three parameters. However, the percentage ASE gain resulting from a unit increase in p_{UE} is far less as

compared to the ASE gains achieved from increasing ζ and λ_{RRH}. Moving on to multi-tier EE, we observe no visible trend with p_{UE}. Just like the single tier network, the EE behaves in the exact opposite fashion as compared to ASE with variation in RRH density. As the S-cell size increases from $\zeta = 0.1$ to $\zeta = 0.4$, we observe almost 4 times gains in EE. However, on further increment to $\zeta = 0.5$, there is a decrease in EE for all four network configurations involving different p_{UE} and λ_{RRH} combinations. Although larger S-cell sizes increase the sum throughput due to a high proportion of UEs connected to mmWave RRHs, this is accompanied by a higher percentage of NLOS mmWave links. The high pathloss associated with NLOS mmWave connections limits the throughput gains which is eventually overshadowed by the additional power consumption due to a higher number of activated RRHs. The results in Fig. 12 once again re-emphasize the need of an optimization framework within an intelligent SON engine integrated in a central entity to dynamically adjust ζ, p_{UE} and λ_{RRH} and maximize the formulated network wide ASE-EE tradeoff utility. Future extensions of this work will be dedicated to designing such an optimization framework, and evaluation of its convexity and ability to yield global optima for a pre-fixed range of investigated design parameters.
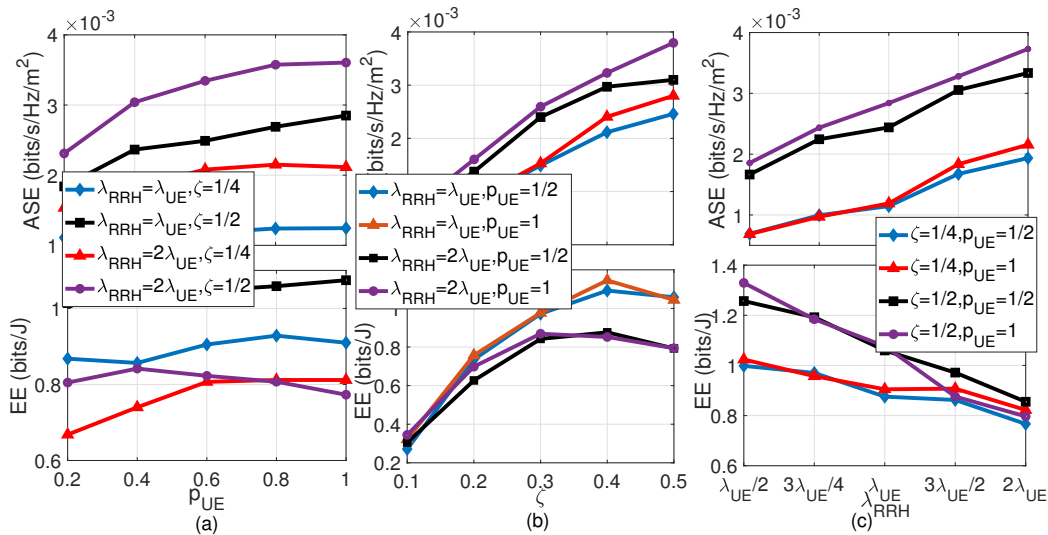

Fig. 12: ASE and EE trends with different p_{UE}, ζ and λ_{RRH} values.

VIII. Conclusion

In this paper, we proposed a user-centric Stienen cell network architecture capable of offering higher system capacity and improved received signal quality in dense deployment scenarios, compared to non user-centric conventional cellular architectures. Since current models for cellular network performance analysis are not applicable to the proposed architecture, we developed a

comprehensive statistical framework for analytical characterization of the area spectral efficiency and energy efficiency of the novel cellular architecture. We presented user-centric scheduling schemes for two network layouts: i) a single-tier network where each UE is served by a single mmWave RRH that resides within its S-cell, and ii) a multi-tier network with a sub-6 GHz macro base station tier overlaid on top of the mmWave RRH tier. While mmWave RRHs are dedicated to serve users in close proximity, the users with void Stienen cells are connected to the macro BSs in the multi-tier design, resulting in a higher average user quality of experience. We further characterized the distance distribution between an arbitrary UE and the angularly interfering RRHs that cause significant interference within mmWave networks.

Our analysis validates the usefulness of the proposed architecture in the form of large SINR gains achieved by virtue of minimizing interference within virtual Stienen zones around scheduled users. We also observed higher network level capacity and lower scheduling delays when compared with a benchmark user-centric architecture from literature. Numerical results based on the derived expressions reveal practical design insights by characterizing the interplay among three design parameters namely S-cell size, user service probability and RRH density; and the network wide KPIs; i.e. ASE and EE. It is observed that the ASE and EE show contrasting results with respect to variations in the design parameters. Therefore, to fully optimize a network efficiency metric, we advocate a SON enabled entity that is capable of dynamic adaptation of the modeling parameters to offer higher throughput or optimal energy utilization, whichever is desired by the network operator in a given spatio-temporal region. From the simulations, the proposed architecture is shown to provide following advantages as compared to the current dense network deployments and a benchmark user-centric scheme: i) SINR gain ranging from 40 dB to 65 dB as compared to current ultra-dense network deployments, ii) 20% reduction in mean scheduling latency, and iii) flexibility of dynamic load balancing between MBS and mmWave RRH tier and setting the ASE-EE tradeoff level by adjustment in design parameters. The proposed work is expected to pave the way for enabling higher capacity and sub-milli second latency for time critical applications in 5G wireless networks. In particular, the reduced latency in the UE scheduling will allow the network to cater to a larger number of devices (both mobile phones and IoT sensors) in an interference free propagation environment.

APPENDIX A

Proof of Proposition I: The probability that the distance between an arbitrary UE and its ith nearest angular interferer is at least r is essentially the probability that there exist exactly $i - 1$

angular interferers inside the circular region of area πr^2 around that UE. Mathematically, it is expressed as

$$F_{r_i}(r) = 1 + \frac{(\lambda_{\text{AIRRH}} \pi r^2)}{(i-1)!} \exp(-\lambda_{\text{AIRRH}} \pi r^2), \tag{33}$$

where λ_{AIRRH} is the mean intensity of the PPP Π_{AIRRH} representing angularly interfering RRHs around an arbitrary UE. For characterization of λ_{AIRRH}, we first define Π_{IRRH} which is the PPP representing interfering RRHs, i.e. activated RRHs outside a UE's S-cell. Due to 1-1 UE-RRH association, the distribution of interfering RRHs is identical to the served UEs. Using Slivnyak's theorem [24], we can express the mean intensity of Π_{IRRH} represented by λ_{IRRH} as $\lambda_{\text{IRRH}} = \lambda_{\text{UE}}^{\text{EF}} = p_{\text{UE}}(1 - p_{\text{emp}})\lambda_{\text{UE}}$.

Now, the angularly interfering RRHs is simply a subset of interfering RRHs containing the RRHs having completely aligned antenna beams with the considered UE. This implies that Π_{AIRRH} is a thinned version of Π_{RRH}. Stating more precisely, the mean intensity of the number of angularly interfering RRHs to an arbitrary UE is dependent on the following factors:

- The number of UEs scheduled for service per unit area, which is controllable by an adjustable parameter p_{UE}.
- The probability that the Stienen cell around a UE would have an RRH within its covered area. The size of the Stienen cell is adjustable via ζ.
- The probability that the antenna bore-sights of a UE and an activated RRH outside its S-cell are completely aligned.

Keeping the stated conditions in consideration, the mean intensity of Π_{AIRRH} is expressed as

$$\lambda_{\text{AIRRH}} = \frac{p_{\text{UE}}\lambda_{\text{UE}}(1 - p_{\text{emp}})\theta_{\text{UE}}\theta_{\text{RRH}}}{(2\pi)^2}. \tag{34}$$

Substituting (34) in (33) and differentiating to find the probability density function yields (10). Note that for omni-directional transmission, Π_{AIRRH} essentially converges to Π_{IRRH}, which is the union of angularly interfering RRHs and interfering RRHs with misaligned antenna beams with UE.

APPENDIX B

Proof of Theorem I: The SINR coverage probability for an arbitrary UE can be expressed as

$$P_{cov}(\gamma_{th}) = \mathbb{P}(\text{SINR} > \gamma_{th}) = \mathbb{P}(h_o > \frac{\gamma_{th}(\sigma^2 + \mathbb{I})}{G_{\text{UE}}G_{\text{RRH}}PL(r_o)}), \tag{35}$$

where $\sigma^2 + \mathbb{I}$ is the summation of noise and interference given as denominator in (11). Since h_o is considered to be a normalized Gamma random variable, we employ Alzer's Lemma [30] to modify (35) as

$$P_{cov}(\gamma_{th}) = \sum_{n=1}^{N} (-1)^{n+1} \binom{N}{n} \mathbb{E}\left(\exp(\frac{-n\eta\gamma_{th}(\sigma^2 + \mathbb{I})}{G_{\text{UE}}G_{\text{RRH}}PL(r_o)})\right), \tag{36}$$

where $\eta = N(N!)^{-\frac{1}{N}}$ and N is the parameter for h_o and takes the value of N_{L} (or N_{N}) depending upon whether the serving RRH is within the LOS (or NLOS) region. The noise and interference components can be treated distinctly as

$$P_{cov}(\gamma_{th}) = \sum_{n=1}^{N} (-1)^{n+1} \binom{N}{n} \mathbb{E}\left(\exp(\frac{-n\eta\gamma_{th}(\sigma^2)}{G_{\mathrm{UE}}G_{\mathrm{RRH}}PL(r_{\boldsymbol{o}})})\right) \mathbb{E}\left(\exp(\frac{-n\eta\gamma_{th}(\mathbb{I})}{G_{\mathrm{UE}}G_{\mathrm{RRH}}PL(r_{\boldsymbol{o}})})\right),$$

$$\overset{(a)}{=} \sum_{n=1}^{N} (-1)^{n+1} \binom{N}{n} \mathbb{E}\left(\exp(\frac{-n\eta(\sigma^2)}{G_{\mathrm{UE}}G_{\mathrm{RRH}}PL(r_{\boldsymbol{o}})})\right) L_{\mathbb{I}}\left(\frac{-n\eta\gamma_{th}}{G_{\mathrm{UE}}G_{\mathrm{RRH}}PL(r_{\boldsymbol{o}})}\right),$$

(37)

where (a) follows from the Laplace functional of the interference, i.e. $L_{\mathbb{I}}(s) = \mathbb{E}\left(\exp(-s\mathbb{I})\right)$. To evaluate $L_{\mathbb{I}}(s)$, we can split the interfering RRHs into LOS and NLOS considering the distribution of distance from an arbitrary UE to LOS interferers and NLOS interferers is only weakly dependent [18]. Hence, if we assume Φ_{ILOS} and Φ_{INLOS} to be the PPPs of the interfering RRHs within LOS and NLOS regions respectively, then by applying the independence property, (37) becomes

$$P_{cov}(\gamma_{th}) = \sum_{n=1}^{N} (-1)^{n+1} \binom{N}{n} \mathbb{E}\left(\exp(\frac{-n\eta\gamma_{th}(\sigma^2)}{G_{\mathrm{UE}}G_{\mathrm{RRH}}PL(r_{\boldsymbol{o}})})\right) L_{\mathbb{I}_{\mathrm{L}}}(\frac{-n\eta_{\mathrm{L}}\gamma_{th}}{G_{\mathrm{UE}}G_{\mathrm{RRH}}PL(r_{\boldsymbol{o}})}) L_{\mathbb{I}_{\mathrm{N}}}(\frac{-n\eta_{\mathrm{N}}\gamma_{th}}{G_{\mathrm{UE}}G_{\mathrm{RRH}}PL(r_{\boldsymbol{o}})}).$$

(38)

Let us consider that the arbitrary UE under consideration is being served by an RRH within its LOS region (i.e. $r \leq R_o$). Now, the interfering RRHs could be in either the LOS or the NLOS region. For interferers in the LOS region, the Laplace functional of the interference in (38) is calculated as

$$L_{\mathbb{I}_{\mathrm{L}}}(\frac{-n\eta_{\mathrm{L}}\gamma_{th}}{G_{\mathrm{UE}}G_{\mathrm{RRH}}PL(r_{\boldsymbol{o}})}) = \mathbb{E}\left(\exp(\frac{-n\eta_{\mathrm{L}}\gamma_{th}r^{\alpha_{\mathrm{LOS}}}\sum_{i\in\Phi_{\mathrm{ILOS}}}|h_i|^2 G_i r_i^{-\alpha_{\mathrm{LOS}}}}{G_{\mathrm{UE}}G_{\mathrm{RRH}}})\right)$$

$$\overset{(b)}{=} \exp\left(-2\pi\lambda_{\mathrm{IRRH}}\sum_{k=1}^{4} b_k \int_r^{R_o} [1 - \mathbb{E}_{h_i}(\exp\{-n\eta_{\mathrm{L}}\gamma_{th}h_i\bar{a}_k(r/t)^{\alpha_{\mathrm{LOS}}}\})t\mathrm{d}t]\right),$$

(39)

where the directivity gain of the interfering RRH G_i is evaluated by considering it as a discrete random variable [17]. Note that we have assumed the pathloss intercepts for both LOS and NLOS scenarios as unity. Further, (b) follows from computing the Laplace functional of Φ_{ILOS}. Finally, by computing the moment generating function of the normalized gamma random variable h_i, we obtain

$$L_{\mathbb{I}_{\mathrm{L}}}(\frac{-n\eta_{\mathrm{L}}\gamma_{th}}{G_{\mathrm{UE}}G_{\mathrm{RRH}}PL(r_{\boldsymbol{o}})}) = \exp\left[-2\pi\lambda_{\mathrm{IRRH}}\sum_{k=1}^{4} b_k \int_r^{R_o} F\left(N_{\mathrm{L}}, \frac{n\eta_{\mathrm{L}}\bar{a}_k\gamma_{th}r^{\alpha_{\mathrm{LOS}}}}{N_{\mathrm{L}}t^{\alpha_{\mathrm{LOS}}}}\right)t\mathrm{d}t\right] = \exp\left[-I_{\mathrm{LL}}(\gamma_{th},r)\right]. \quad (40)$$

In a similar manner, the Laplace functional of the NLOS interfering RRHs for this UE is given by

$$L_{\mathbb{I}_{\mathrm{N}}}(\frac{-n\eta_{\mathrm{N}}\gamma_{th}}{G_{\mathrm{UE}}G_{\mathrm{RRH}}PL(r_{\boldsymbol{o}})}) = \exp\left[-2\pi\lambda_{\mathrm{IRRH}}\sum_{k=1}^{4} b_k \int_r^{R_o} F\left(N_{\mathrm{N}}, \frac{n\eta_{\mathrm{L}}\bar{a}_k\gamma_{th}r^{\alpha_{\mathrm{LOS}}}}{N_{\mathrm{N}}t^{\alpha_{\mathrm{NLOS}}}}\right)t\mathrm{d}t\right] = \exp\left[-I_{\mathrm{LN}}(\gamma_{th},r)\right]. \quad (41)$$

Now for a UE served by an RRH in the NLOS region, it is intuitive to observe that $\Phi_{\mathrm{ILOS}} = \emptyset$, therefore, the Laplace functional

$$L_{\mathbb{I}_{\mathrm{L}}}(\frac{-n\eta_{\mathrm{L}}\gamma_{th}}{G_{\mathrm{UE}}G_{\mathrm{RRH}}PL(r_{\boldsymbol{o}})}) = \exp[-I_{\mathrm{LN}}(\gamma_{th},r)] = 1.$$

(42)

Similar to (41), we derive the Laplace functional of the NLOS interferes as

This article has been accepted for publication in a future issue of this journal, but has not been fully edited. Content may change prior to final publication. Citation information: DOI 10.1109/TGCN.2020.2967888, IEEE Transactions on Green Communications and Networking

31

$$L_{\mathbb{I}_{\mathrm{N}}}\left(\frac{-n\eta_{\mathrm{N}}\gamma_{th}}{G_{\mathrm{UE}}G_{\mathrm{RRH}}PL(r_o)}\right) = \exp\left[-2\pi\lambda_{\mathrm{IRRH}}\sum_{k=1}^{4}b_k\int_r^\infty F\left(N_{\mathrm{N}}, \frac{n\eta_{\mathrm{N}}\bar{a_k}\gamma_{th}r^{\alpha_{\mathrm{NLOS}}}}{N_{\mathrm{N}}t^{\alpha_{\mathrm{NLOS}}}}\right)t\mathrm{dt}\right] = \exp\left[-I_{\mathrm{LN}}(\gamma_{th},r)\right].$$

(43)

Finally, integrating over $f_{r_o}(r)$ for LOS and NLOS regions and by summation of coverage probabilities for each region, we obtain (12).

ACKNOWLEDGEMENT

REFERENCES

[1] J. G. Andrews, X. Zhang, G. D. Durgin, and A. K. Gupta, "Are we approaching the fundamental limits of wireless network densification?" *IEEE Communications Magazine*, vol. 54, no. 10, pp. 184–190, October 2016.

[2] S. Chen, F. Qin, B. Hu, X. Li, and Z. Chen, "User-centric ultra-dense networks for 5G: challenges, methodologies, and directions," *IEEE Wireless Communications*, vol. 23, no. 2, pp. 78–85, April 2016.

[3] S. Zaidi, A. Imran, D. McLernon, and M. Ghogho, "Characterizing Coverage and Downlink Throughput of Cloud Empowered HetNets," *Communications Letters, IEEE*, vol. PP, no. 99, pp. 1–1, 2015.

[4] U. Hashmi, S. A. R. Zaidi, A. Darbandi, and A. Imran, "On the efficiency tradeoffs in User-Centric cloud RAN," in *IEEE ICC 2018 Next Generation Networking and Internet Symposium (ICC'18 NGNI)*, Kansas City, USA, May 2018.

[5] U. S. Hashmi, A. Islam, K. M. Nasr, and A. Imran, "Towards User QoE-Centric Elastic Cellular Networks: A Game Theoretic Framework for Optimizing Throughput and Energy Efficiency," in *2018 IEEE 29th Annual International Symposium on Personal, Indoor and Mobile Radio Communications (PIMRC)*, Sep. 2018, pp. 1–7.

[6] J. Stienen, *Die Vergroeberung von Karbiden in reinen Eisen-Kohlenstoff-Staehlen.* na, 1982.

[7] M. R. Akdeniz, Y. Liu, M. K. Samimi, S. Sun, S. Rangan, T. S. Rappaport, and E. Erkip, "Millimeter Wave Channel Modeling and Cellular Capacity Evaluation," *IEEE Journal on Selected Areas in Communications*, vol. 32, no. 6, pp. 1164–1179, June 2014.

[8] A. Mohamed, O. Onireti, M. A. Imran, A. Imran, and R. Tafazolli, "Control-Data Separation Architecture for Cellular Radio Access Networks: A Survey and Outlook," *IEEE Communications Surveys Tutorials*, vol. 18, no. 1, pp. 446–465, Firstquarter 2016.

[9] Y. Zhang and Y. J. Zhang, "User-centric virtual cell design for Cloud Radio Access Networks," in *Signal Processing Advances in Wireless Communications (SPAWC), 2014 IEEE 15th International Workshop on*, June 2014, pp. 249–253.

[10] S. Buzzi and A. Zappone, "Downlink power control in user-centric and cell-free massive mimo wireless networks," in *2017 IEEE 28th Annual International Symposium on Personal, Indoor, and Mobile Radio Communications (PIMRC)*, Oct 2017, pp. 1–6.

[11] M. Alonzo, S. Buzzi, A. Zappone, and C. DElia, "Energy-Efficient Power Control in Cell-Free and User-Centric Massive MIMO at Millimeter Wave," *IEEE Transactions on Green Communications and Networking*, vol. 3, no. 3, pp. 651–663, Sep. 2019.

[12] M. Di Renzo, A. Zappone, T. T. Lam, and M. Debbah, "System-Level Modeling and Optimization of the Energy Efficiency in Cellular NetworksA Stochastic Geometry Framework," *IEEE Transactions on Wireless Communications*, vol. 17, no. 4, pp. 2539–2556, April 2018.

[13] M. D. Renzo, A. Zappone, T. T. Lam, and M. Debbah, "Spectral-Energy Efficiency Pareto Front in Cellular Networks: A Stochastic Geometry Framework," *IEEE Wireless Commun. Letters*, vol. 8, no. 2, pp. 424–427, 2019. [Online]. Available: https://doi.org/10.1109/LWC.2018.2874642

[14] R. Hernandez-Aquino, S. A. R. Zaidi, M. Ghogho, D. McLernon, and A. Swami, "Stochastic geometric modeling and analysis of non-uniform two-tier networks: A stienen's model-based approach," *IEEE Transactions on Wireless Communications*, vol. 16, no. 6, pp. 3476–3491, June 2017.

[15] M. D. Renzo, "Stochastic Geometry Modeling and Analysis of Multi-Tier Millimeter Wave Cellular Networks," *IEEE Transactions on Wireless Communications*, vol. 14, no. 9, pp. 5038–5057, Sept 2015.

[16] T. Bai and R. W. Heath, "Coverage and Rate Analysis for Millimeter-Wave Cellular Networks," *IEEE Transactions on Wireless Communications*, vol. 14, no. 2, pp. 1100–1114, Feb 2015.

[17] J. G. Andrews, T. Bai, M. N. Kulkarni, A. Alkhateeb, A. K. Gupta, and R. W. Heath, "Modeling and analyzing millimeter wave cellular systems," *IEEE Transactions on Communications*, vol. 65, no. 1, pp. 403–430, Jan 2017.

[18] O. Onireti, A. Imran, and M. A. Imran, "Coverage, Capacity and Energy Efficiency Analysis in the Uplink of mmWave Cellular Networks," *IEEE Transactions on Vehicular Technology*, pp. 1–1, 2017.

[19] T. S. Rappaport, G. R. MacCartney, M. K. Samimi, and S. Sun, "Wideband Millimeter-Wave Propagation Measurements and Channel Models for Future Wireless Communication System Design," *IEEE Transactions on Communications*, vol. 63, no. 9, pp. 3029–3056, Sept 2015.

[20] A. Imran, M. A. Imran, A. Abu-Dayya, and R. Tafazolli, "Self Organization of Tilts in Relay Enhanced Networks: A Distributed Solution," *IEEE Transactions on Wireless Communications*, vol. 13, no. 2, pp. 764–779, February 2014.

[21] K. Roth, H. Pirzadeh, A. L. Swindlehurst, and J. A. Nossek, "A Comparison of Hybrid Beamforming and Digital Beamforming With Low-Resolution ADCs for Multiple Users and Imperfect CSI," *IEEE Journal of Selected Topics in Signal Processing*, vol. 12, no. 3, pp. 484–498, June 2018.

[22] J. G. Andrews, F. Baccelli, and R. K. Ganti, "A Tractable Approach to Coverage and Rate in Cellular Networks," *IEEE Transactions on Communications*, vol. 59, no. 11, pp. 3122–3134, November 2011.

[23] M. Haenggi, "On distances in uniformly random networks," *IEEE Transactions on Information Theory*, vol. 51, no. 10, pp. 3584–3586, Oct 2005.

[24] J. M. D. Stoyan, W. S. Kendall and L. Ruschendorf, *Stochastic geometry and its applications*. Wiley Chichester, 1995, vol. 2.

[25] G. Auer, V. Giannini, C. Desset, I. Godor, P. Skillermark, M. Olsson, M. Imran, D. Sabella, M. Gonzalez, O. Blume, and A. Fehske, "How much energy is needed to run a wireless network?" *Wireless Communications, IEEE*, vol. 18, no. 5, pp. 40–49, October 2011.

[26] R. Gupta, E. Calvanese Strinati, and D. Ktenas, "Energy efficient joint DTX and MIMO in cloud Radio Access Networks," in *Cloud Networking (CLOUDNET), 2012 IEEE 1st International Conference on*, Nov 2012, pp. 191–196.

[27] S. H. Lim, J. Bae, S. Kim, B. Shim, and J. W. Choi, "Efficient Beam Training and Channel Estimation for Millimeter Wave Communications Under Mobility," *ArXiv*, vol. abs/1804.07973, 2018.

[28] U. S. Hashmi, S. A. R. Zaidi, and A. Imran, "User-Centric Cloud RAN: An Analytical framework for Optimizing Area Spectral and Energy Efficiency," *IEEE Access*, pp. 1–1, 2018.

[29] R. Jain, D.-M. Chiu, and W. Hawe, "A quantitative measure of fairness and discrimination for resource allocation in shared computer systems," *CoRR*, vol. cs.NI/9809099, 1998.

[30] H. Alzer, "On some inequalities for the incomplete gamma function," *Mathematics of Computation*, vol. 66, no. 218, pp. 771–778, 1997. [Online]. Available: http://www.jstor.org/stable/2153894